Experimentally validated finite element modeling of linear alternators for predicting electrical power and electromagnetic force due to resistive loads

by

Bryce Alan Teaford

B.S., Kansas State University, 2021

A THESIS

submitted in partial fulfillment of the requirements for the degree

MASTER OF SCIENCE

Alan Levin Department of Mechanical and Nuclear Engineering
Carl R. Ice College of Engineering

KANSAS STATE UNIVERSITY
Manhattan, Kansas

2023

Approved by:

Major Professor
Dr. Jared D. Hobeck

Copyright

Abstract

High energy density conversion systems (HEDCS) have been of growing interest within the scientific community. The applications of these HEDCS in the aerospace industry are seemingly unending as they can be small and lightweight compared to current energy conversion systems. NASA's use of unmanned aerial vehicles (UAV) in everyday scientific study and operations creates a need for an energy efficient method of operating these aircraft. While these UAVs have already been proven useful on Earth, NASA's discovery of materials on Mars that can perform a combustion cycle, namely O_2 and CH_4, creates an outlet for implementing HEDCS on future Mars UAVs as well. Working in tandem with Wichita State University, Kansas University, Pulse Aerospace, Aerojet Rocketdyne, and NASA Glenn Research Center with NASA funding, the objective of this project was to develop a design methodology for cost-efficient HEDCS. Previous efforts of the research team led to the decision of designing a miniature internal combustion engine (MICE) with a free piston architecture coupled to a linear alternator. This architecture was chosen because of the inherent high efficiency they demonstrate compared to common internal combustion engines resulting in a system with less friction loss and a more compact design. After the physical design of a MICE was decided, a mathematical model for predicting optimal engine performance was needed. A portion of the research team developed a model for engine kinematics and combustion dynamics. The research in this thesis focuses on attaining and validating model parameters that will be used to couple the aforementioned engine model to an electromechanical alternator model. As the magnets (mover) of a linear alternator pass through the coils (stator) an electrical current is generated in the coil along with an electromagnetic force that opposes the magnet motion. This force is similar to a damping force

and is directly proportional to velocity of the mover. To create a comprehensive electromagnetic model for the linear alternator that can be integrated with the engine dynamics models, the time series values for power generation and this electromagnetic force must be found. This work details experimental methods used to validate finite element analysis (FEA) predictions of the relationships between power, resistive load, force, and mover velocity in a simple permanent magnet linear alternator. An experiment that could measure these values of interest whose motion could also be modeled in the electromagnetic simulation software, EMWorks, was developed. Two experiments were run, a drop test and a shaker table experiment. The drop test experiment consisted of a permanent magnet being dropped through a coil while the magnet motion and the coil voltage across a resistive load was collected. This experiment proved to be a useful venture as it helped with learning the basics of the simulation software and provided a power output comparison but could not provide a reliable acceleration measurement from the collected velocity data to calculate the opposing force. The shaker table experiment was used to imitate a linear alternator by oscillating the magnet in a coil while measuring the same values as the drop test in addition to measuring force directly with a statically and dynamically calibrated load cell. Through comparisons of this experimental and simulated data, the finite element model was validated for use in predicting power generation and the electromagnetic force acting against the mover of a linear alternator providing the means necessary to create a comprehensive MICE alternator model.

Table of Contents

List of Figures

List of Tables

Acknowledgements

I would first like to thank Professor Jared D. Hobeck for giving me this opportunity to work with him. I am very grateful for him and everything he has taught me. I have learned so much about who I am as an engineer and what I need to do to become an even better one moving forward. I will continuously apply what I learned from Dr. Hobeck in my everyday life and am glad I met him. Also, I extend a great thanks to my research committee, Dr. Behrooz Mirafzal and Dr. Jack Xin, for overseeing the completion of my thesis.

I would also like to thank the team and their respective organizations who proposed this project: Dr. Sindu Preetham Burugupally (Wichita State University), Dr. Christopher Depcik (Kansas University), Bill Donovan (Pulse Aerospace), Dr. Fisher (Aerojet Rocketdyne), and Lee Mason (NASA Glenn Research Center). Without their early work, this project would not exist. Likewise, I thank NASA for approving and funding this project and EMWorks for allowing me to work with their software.

In addition, I would like to thank my friends and family. I would not be the person I am today without them. I am lucky to have each and every one of them and I thank God for putting them in my life. Within this group, I would like to personally thank Tyler Kodanaz for discussing seemingly random basic electrical engineering topics with me as I worked on this thesis as well as Molly Mulqueen for her loving emotional support along the way.

These acknowledgments would not feel complete without directly thanking my two beautiful sisters, Ashley and Heather who have both supported me throughout the most challenging times in my life and have always been quick to offer help whenever I needed it. For all the times they fed me, let me crash on their couch, helped me find work for the summer, and all the other things they did for me during my college career, I thank them greatly.

Lastly, but certainly not least, I thank my parents Mike and Jackie Teaford. I am forever grateful for their loving support. If it was not for them, I would not be where I am now. I owe everything I am to them and will never be able to express how much their support has meant to me. All I can say is that I love them both and thank them for being the greatest parents I could have ever asked for.

Dedication

~ Dedicated to the memory of my grandma ~

Maryetta Herring-Teaford, B.S., Horticulture Therapy

Kansas State University Class of 1987

Chapter 1

Introduction and Literature Review

1.1 Introduction

The use of unmanned aerial vehicles (UAV) in the scientific community has become a common research tool for data collection and everyday operations. Currently, the most widely used method to power smaller UAVs is to implement rechargeable battery packs, mainly lithium-ion type packs, in the powertrain. Comparison of the possible flight times for a common UAV powered by these packs and other power plants has shown the pitfalls of using lithium-ion [1]. This study displayed that the implementation of an internal combustion engine (ICE) in smaller UAVs can generate longer flight times. The ICE coupled to an alternator must convert heat to electrical energy with an energy output to powertrain volume ratio (energy density) higher than the original battery pack powertrain itself to achieve these flight times. The term high energy density conversion system (HEDCS) is characterized as having an energy density greater than 500 Wh/L [2]. By designing a HEDCS, it can be implemented on smaller UAVs to increase their flight times. This would aid the scientific community that uses them for research, such as NASA which implements them for remote sensing, imaging, tracking storms, and communications [3]. In 2020, a proposal to NASA was made to secure funding for a project that encouraged the collaboration between NASA Glenn Research Center, the three major Kansas universities, Wichita State, Kansas, and Kansas State (KSU), and two industry partners Pulse Aerospace and

Aerojet Rocketdyne to design a HEDCS for Earth and Mars UAVs that could output power in the range of 0.25-1 kW. The main objective of this team project was broken down into four criteria which are listed in Table 1.1 along with previous work by the team cited as well. KSU's task was to validate a method to predict the properties of the system alternator used for electrical power generation that will affect the overall performance of the HEDCS.

Table 1.1. The main criteria needed to be met to complete the team project.

Criteria	Relevant Work
Deriving a zero-dimensional (0-D) model of MICE and analyzing MICE performance against a traditional ICE.	[1]
Electromechanical modeling of integrated linear alternator for optimal load and electrical power output.	This thesis
Simulating the availability of O_2 and CH_4 resources on Mars and building a combustion model.	[4]
Integrating the coupled electromechanical MICE models with the combustion model.	Future work

1.2 Internal Combustion Engine Design

In order to understand how the alternator in this work needed to be modeled, the engine type it would be coupled to had to be known. Previous work by the team investigated the use of ICE powered with hydrogen fuel in different powertrain configurations to prolong the flight times of UAVs [1]. This fuel was picked for the higher mass-based energy density it provides compared to common aviation fuels [5]. Different configurations of how the generated electrical power could be distributed in the system were also discussed. The three investigated configurations with engines consisted of a rotational engine that turned a generator to power the electronics of the UAV and spun the propeller manually, a rotational engine that spun only the propeller with a separate battery pack that powered the electronic propeller motor, and a free piston engine (FPE) with a generator that powered the electronics and propeller motor. Each powertrain option was used to make final decisions for the proposed ICE architecture.

For this ICE to be a HEDCS, it needs to be small enough to fit on a UAV with low losses to friction and heat. This type of engine is referred to as a miniature internal combustion engine (MICE). Of the engines modeled, the architecture chosen for the MICE was a free piston engine coupled to a linear alternator for its inherent compact design and low loss to friction and heat. With the establishment of the materials necessary to conduct a combustion cycle on Mars, O_2 and CH_4, the motivation to model a MICE that could operate on the Martian world was made [6]. After the decision of the final MICE architecture, methods to calculate the performance of engines running on this mixture were developed [4].

1.2.1 Free Piston Architecture

The first modern FPE was designed and marketed by an Argentine engineer, Raul Patreas Pascera, in 1933 [7]. There are many different types of FPEs, but the defining characteristic that sets it apart from conventional engines is that there is no crankshaft connected to the piston as shown in Figure 1.1. By removing the crankshaft, losses to friction are decreased as the piston can move freely in the cylinder while also increasing the power-to-weight ratio [8]. The acceleration of the piston can also be much higher than normal engines yielding better efficiency by moving the piston away from the combustion chamber faster than conventional engines and decreasing heat transfer loss. This motion creates variable compression ratios which allow for different fuels to be used in them, such as CH_4 which was discussed previously. There are three major forces acting on the piston: combustion force, the load device force (usually from an alternator), and the rebound device force. Since the piston motion is not restricted by a crankshaft and only by the devices that make it reciprocate it is necessary that an engine model that accounts for all the forces acting on the piston motion be made.

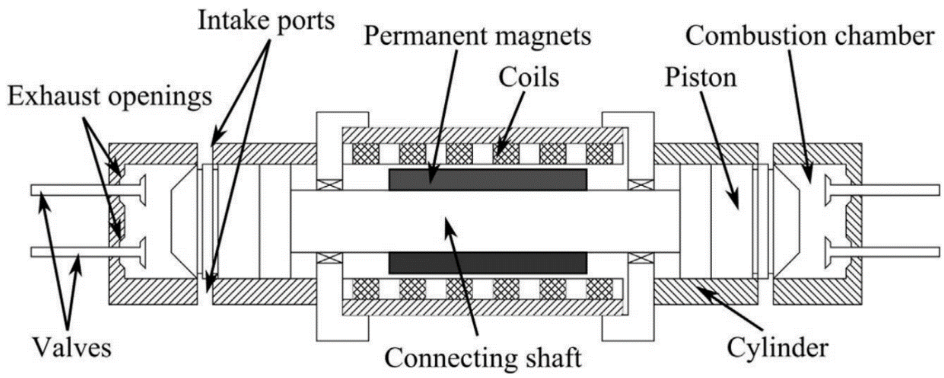

Figure 1.1. Dual piston type free-piston generator [9].

1.2.2 The Linear Alternator

Alternators are generators used to turn mechanical energy into electrical energy. The name alternator comes from the alternating current that they generate before any rectification is done. The most common application for an alternator is the one that powers the electronics and charges the battery in cars [10]. Using the rotational motion from a car engine, magnets are moved in relation to a coil to generate an electromotive force (EMF) through induction [11]. This EMF created is directly proportional to the magnet velocity that excites it. Linear alternators use this same phenomenon to create electrical power, but with linear motion instead. A key difference between rotational and linear alternators are that rotational alternators are separate from the pistons that drive the motion of the system while linear alternator magnets are placed directly on the piston. When this power is generated, an electromagnetic field is created by the current in the coils that acts against the permanent magnetic field of the magnets according to Lenz's law [12]. This creates a force that opposes the magnet motion and is proportional to the magnet velocity. For a FPE, this force can have significant influence on piston dynamics and overall engine performance. This makes it imperative that the electromagnetic force acting against the magnet (mover) from the coil (stator) be considered along with the electrical power output when modeling and designing these engines.

1.3 Mathematical Modeling of the Free Piston Engine Motion

The mechanical vibrations subject is a subset of dynamics that deals with the oscillatory motion of systems. A FPE operates by applying combustion and rebound forces on the piston to make it oscillate back and forth in the cylinder. Forces that are proportional to the velocity of a system and work against the motion are defined as viscous damping forces in mechanical vibrations [13]. Since the electromagnetic force acting against the motion of the mover from the linear alternator behaves as a nonlinear damping force, the electromechanical model can be integrated with the engine models using numerical methods common in the subject of mechanical vibrations [14]. These numerical methods model the oscillatory motion as a mass-spring-damper system as shown in Figure 1.2. The control volume is the area where the CH_4 and O_2 mixture is ignited, creating the combustion force that sets the piston mass in motion while the spring is the rebound force that makes it oscillate. This oscillatory motion is subjected to both linear and nonlinear damping forces. The combustion dynamics and kinematics engine models made by the team already account for the control volume, spring, and viscous damping in the system.

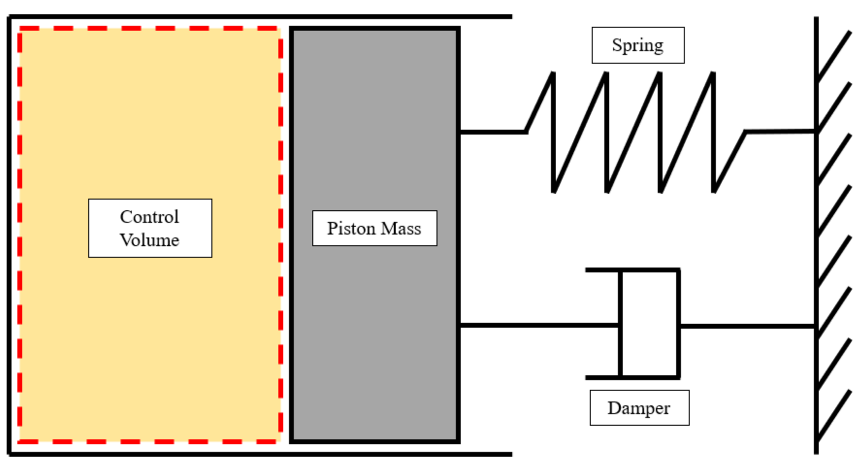

Figure 1.2. The mass-spring-damper system with a hollow cylinder containing the fuel-oxygen mixture used to model the motion of the piston.

The nonlinear damping is the force that the linear alternator imposes against the piston motion and is what this thesis focuses on modelling. This alternator damping is the electromagnetic force from the coil working against the motion of the magnets connected to the piston. By supplying a way to model this force, the values necessary for the team to complete the numerical model of the free piston motion are provided and can be implemented in designing the MICE.

1.4 Existing Linear Alternator Research

Previous work has investigated the performance of linear alternators and how they can be modeled. NASA has demonstrated the ability of Gideon Associate's Sage one-dimensional modeling software to predict the electrical responses of linear alternators [15]. This study displayed the creation of a model that was tuned with experimental and three-dimensional finite element method (FEM) simulated results of the electrical properties. Using this model, predictions were then made for the performance of the alternator. What this research did not include was a validated model for prediction of the electromagnetic force acting against the mover of the alternator. Khatri and Wang (2020) demonstrated how two-dimensional FEM can be used to design a linear wave energy converter with reduced cogging force [16]. Cogging force is the attraction of the permanent magnets to the iron core in machines like motors and generators. Although this did not validate the use of FEM for the team's purposes, it did show that the FEM software can properly calculate magnetic fields to find the magnetic cogging force. This research gave reason to suggest that a finite element model could calculate electromagnetic forces acting against magnets like the ones in a linear alternator.

1.5 Finite Element Analysis

Finite element analysis (FEA) is a common tool for numerically solving engineering models governed by differential equations. This method is used because a large majority of geometries and engineering problems cannot be solved analytically [17]. Three-dimensional FEA works by deconstructing the virtual model of a physical system down into small, finite elements that create a mesh like the ones shown in Figure 1.3. The mesh is the network of elements that sets the boundary conditions for each individual element at the junctions between them. The mesh element size determines the accuracy of the calculation and is refined as needed until the calculations stop changing according to the element size, meaning they have become independent of the mesh and will not change if refined more.

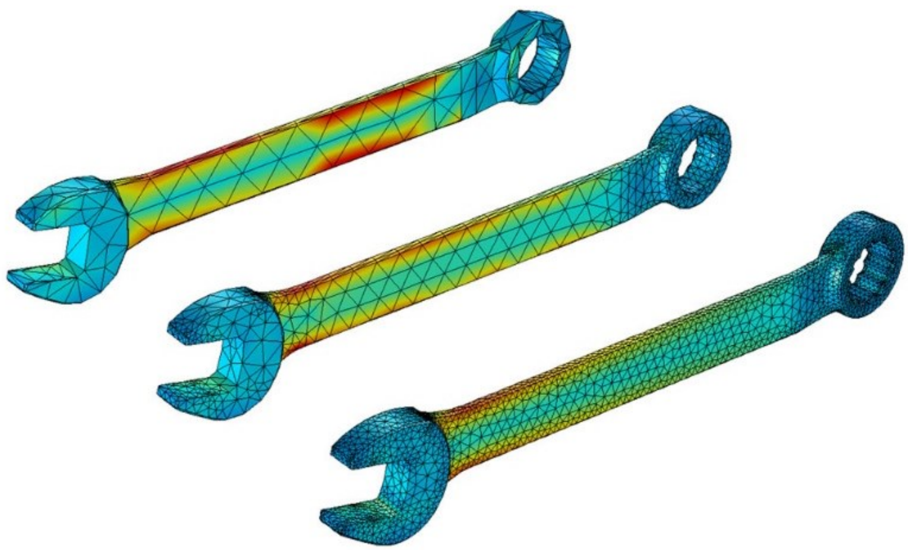

Figure 1.3. The first few iterations of a mesh refinement study of a wrench, transitioning from a coarse mesh to fine (left to right) [17].

1.6 Objectives and Organization of this Thesis

Completion of the proposed project requires that a working model of a high energy density MICE be created. Previous efforts by the research team have created models for predicting the kinematics and combustion dynamics of the engine. The electromechanical properties of a linear alternator that effect the performance of a FPE must be predicted so they can be implemented with the aforementioned models to provide a comprehensive design tool for the MICE. The primary objectives of this thesis are to:

1. Experimentally validate a finite element model of a linear alternator.
2. Characterize the relationships between the electromagnetic force, mover velocity, resistive load, and power output of a linear alternator.

Looking past these primary objectives, this research provides a basis to contribute to the normalized use of free piston engines for power generation. Validating these engine modeling methods will lead to further development of high energy density systems.

This thesis consists of three chapters of original work that reference one another to avoid making repeated statements or definitions. Not including the introduction and literature review in Chapter 1, Chapter 4 serves as a summary of the independent work conducted in this thesis and the recommendation of future work.

Chapter 2 details the methodology behind validating FEA for prediction of the electromechanical properties of linear alternators and uses a preliminary experiment to detail how the FEA software works. The experiment consisted of dropping a disc magnet concentrically through a coil while measuring the coil voltage across a resistive load and the magnet motion to extract the change in velocity from the electromagnetic force. For reasons explained in the chapter, the force could not be reliably calculated from the motion data so only an electrical power comparison was made.

Chapter 3 describes the experimental methods used to measure the electrical power and electromagnetic force acting on an oscillating magnet relative to a coil. The techniques used to measure and calibrate the force sensor are detailed to explain how the data was processed. The experimental results are then compared to FEA simulated data to validate the finite element model for characterizing the relationships between the values under inspection.

Chapter 2

Methodology and Early Work

2.1 Methodology of the Experimental and Finite Element Methods

In studies where a method is used for predicting the values of a physical event, it is important to compare the predicted results to physical measurements, ensuring validity. By comparing the model results to the measurements, the researcher does not only provide proof that the method works but can also find important data on where the method may have pitfalls and must be compensated for. The basic requirements of the experiment needed to validate the finite element model were to generate a measurable coil voltage across a resistive load and electromagnetic force acting against a known relative motion of a permanent magnet passing through a coil, as displayed in Figure 2.1. The direction of magnetization of the magnet had to be perpendicular to the windings while the geometries and positions relative to one another needed to resemble basic linear alternator motion. For the alternator under inspection, the coil needed to be an air core solenoid made of conductive material with enough room for an axially magnetized disc magnet to move through it concentrically. By creating an experiment where motion, coil voltage across a resistive load, and electromagnetic force could be measured, FEA could be used to model it for comparison.

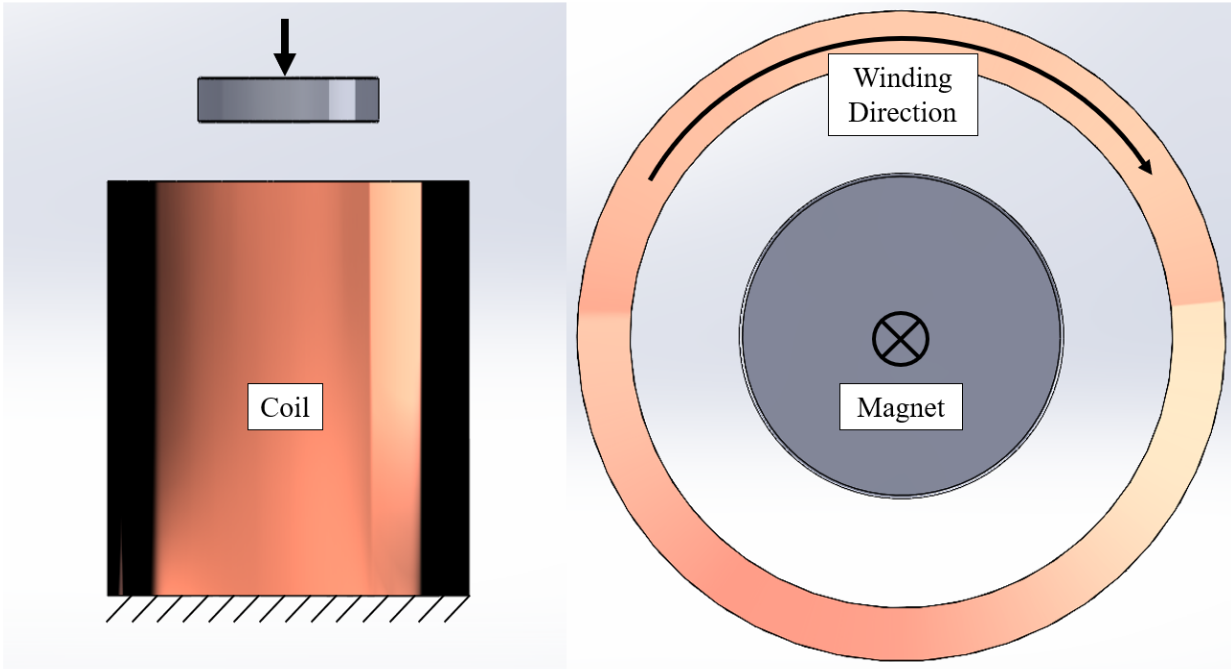

Figure 2.1. The front view (left) and top view (right, zoomed in) of the magnet motion relative to the coil windings desired for the experiment.

Using the SolidWorks electromagnetic simulation software add-in, EMWorks, FEA was performed to model the physical system for comparison of the experimental and simulated results. The realms of both low and high frequency electromagnetics are governed by a set of partial differential equations known as Maxwell's equations [18]. The difference between the two realms is that high frequency electromagnetics must account for displacement currents that are essential to their propagation, while low frequency electromagnetics neglect displacement currents [19]. Generators, like this alternator, fall in the realm of low frequency electromagnetics. For this research, the transient magnetic analysis study type of the software was chosen to model the experiment because it could calculate the change in magnetic fields due to surges in current and magnetic forces. It also had permanent magnet and wound coil simulation capabilities. By using these two methods, a working model for predicting the values of interest could be made.

2.2 Drop Test Experiment

A common experiment used to display the effects of Lenz's law is to drop a magnet down the middle of a copper pipe to watch it fall slowly compared to normal gravitational pull due to the magnetic forces acting against it from the eddy currents generated in the copper. This linear motion and electromagnetic force opposing the magnet motion resembles the alternator movement under inspection. The objective of the drop test experiment in this study was to release the magnet through a wound coil while measuring the coil voltage across different resistive loads in a decade sweep as well as the magnet velocity to extract the change in velocity from the opposing force acting on it. The extracted acceleration would then be used to calculate the force that acted on the magnet.

2.2.1 Structure and General Equipment Information

The drop test structure needed to guide the magnet as it gained speed from gravity until passing through the coil, catching the magnet safely after exiting the coil. The structure consisted of a vertically oriented PVC pipe with a coil wound around a 3D printed body stationed at the bottom as shown in Figure 2.2. The PVC pipe was used to guide the magnet down until it reached the coil body. The body was made to fit the bottom of the guide along with another piece of pipe underneath it that allowed for removeable pins for catching the magnet to be installed. Pins were also positioned at a height of 0.6096 m from the bottom of the guide so the magnet could be dropped from the same distance each time. The motion of the magnet was measured using a doppler vibrometer (Polytec OFV-534) with a vibrometer controller (Polytec OFV-5000) by reflecting the vibrometer laser up into the drop guide with a mirror to keep it out of harm's way if the magnet was not stopped. Figure 2.3 shows the 3D printed casing with a lid and arms that partially spanned the guide diameter used to keep the magnet concentric to the coil as it fell. This casing was stuffed with a cushion under the magnet for protection and had a piece of reflective tape attached to its bottom to aid the vibrometer measurement.

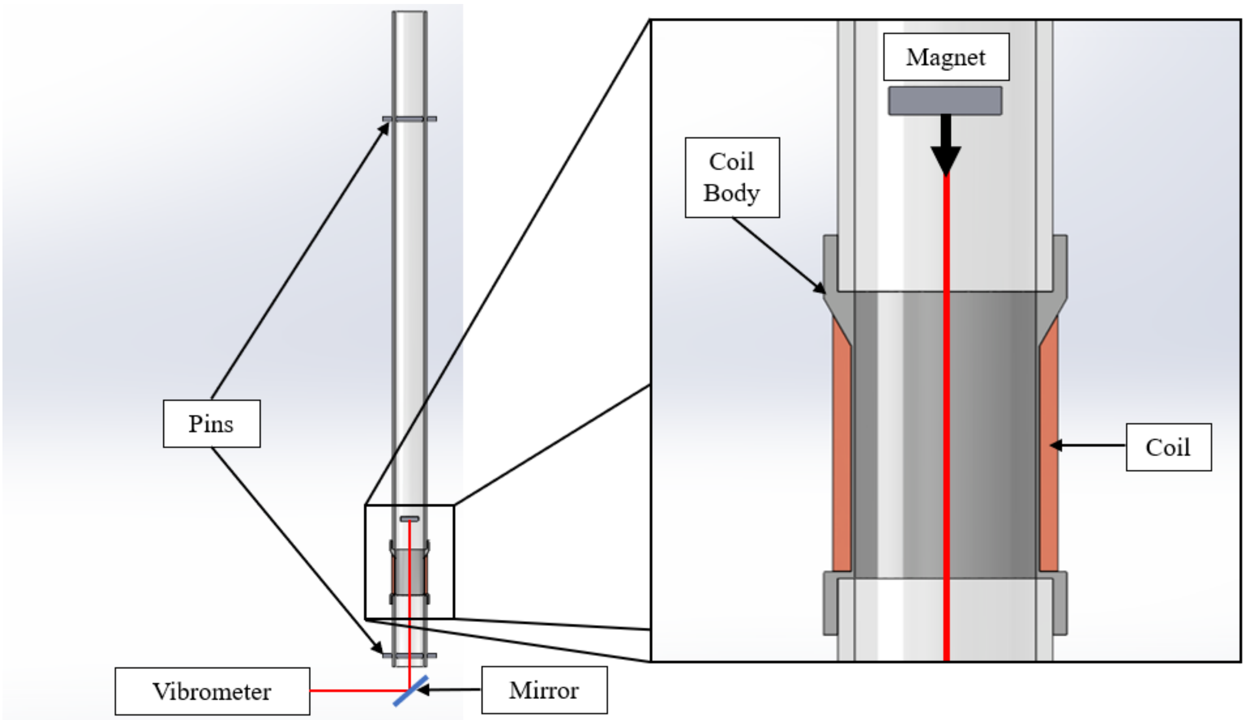

Figure 2.2. Cross section view of the modeled drop test experiment structure displaying how the vibrometer laser was reflected vertically to record the magnet motion.

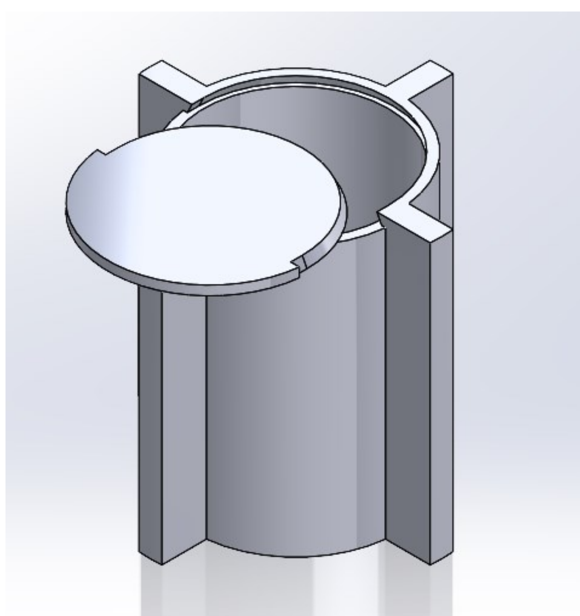
Figure 2.3. Model of magnet protection casing with lid for drop test experiment.

The magnets purchased for this experiment were neodymium disc magnets from KJ Magnetics. Each magnet was 2.54-cm in diameter, with thicknesses varying from 0.3175 to 2.54-cm. These magnets are of the rare earth family and are known to be the most powerful permanent magnets in the world [20]. Their composition, as stated by their name, is mainly neodymium but also consists of iron and boron which causes some to refer to them as NdFeB magnets. The strength of these magnets is rated on a grading scale; the magnets purchased were the highest grade available from KJ Magnetics at N52. This grading information is important for the modeling of magnets and will be discussed further in the chapter for simulation methods.

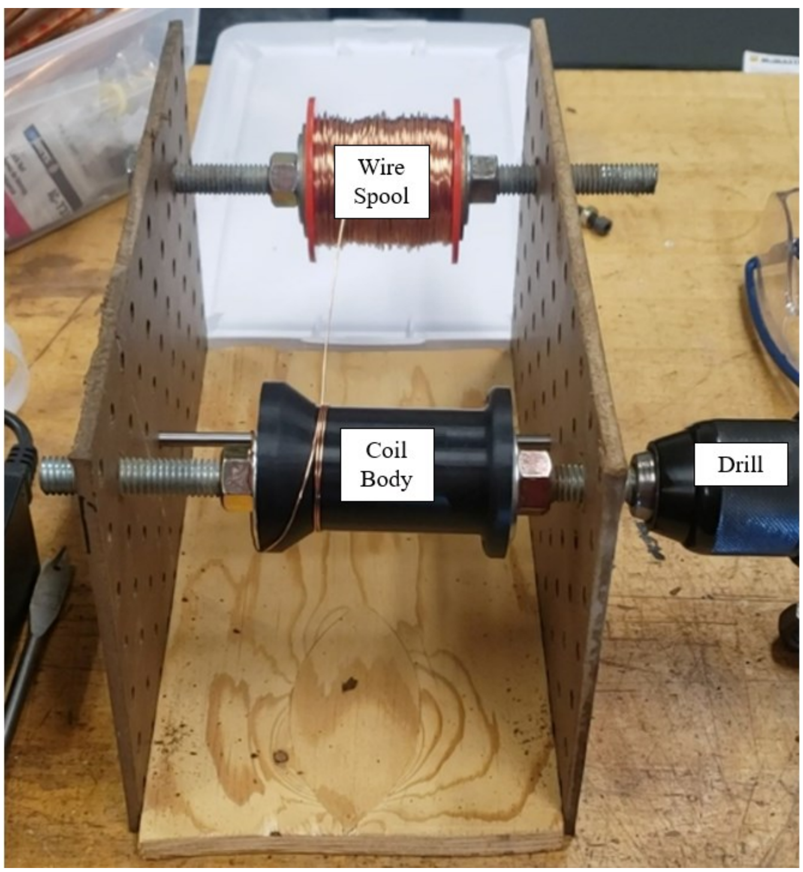

Figure 2.4. The winding apparatus that was used to produce coils for the experiment.

The coil for this experiment was wound using a self-built apparatus that utilized a drill to turn the coil body to pull wire from a spool, winding it around the body with each revolution as shown in Figure 2.4. The jaws of the drill were tightened around a piece of all-thread the coil body was secured to. The all-thread spanned the holes in two pieces of wood that allowed for it to spin with the drill while winding took place. The wire was dispersed across the body, filling each level until moving onto the next layer of wire. After practicing winding the coils, a digital counter (Kesoto Model GDD7949AT-P12V) was implemented to count every revolution of the coil body to record the number of turns in the winding for the experiment. The number of turns and gauge of wire along with the dimensions of the coil are all that are needed to model wound coils in the simulation software.

2.2.2 Experimental Data Collection and Processing

For this experiment, an N52 disc magnet of 0.635-cm thickness was dropped through a 500-turn coil made of 22-gauge copper wire of the dimensions displayed in Appendix A. The vibrometer and voltage across the resistive load time series data was collected using the analog input channels on a USB-6212 DAQ. The vibrometer output velocity-to-voltage proportion was set to 1 (m/s)/V, so no conversion was needed for processing the data. Figure 2.5 diagrams the flow of data from its respective source to the computer and Appendix B shows the LabView VI used to record measurements at a 10 kHz sampling rate. Before testing, the vibrometer was finely focused in the area where the magnet would be inside the coil during the drop to obtain the most accurate velocity values. The coil voltage was measured across different resistive loads in series of a nominal decade sweep from 1 Ohm to 10 MOhm, resulting in eight sets of data for each drop. For every resistance, fifteen drops were conducted to try and account for any variance between them. Every group of fifteen was saved in the same time series file.

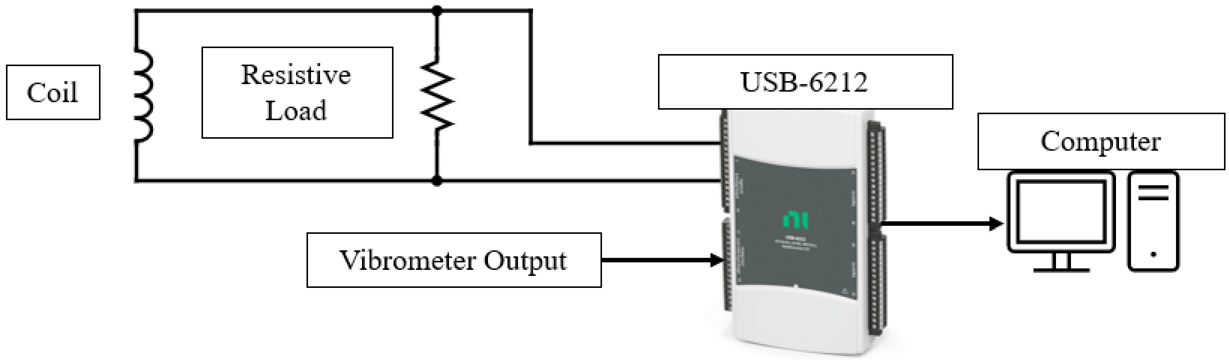

Figure 2.5. Diagram showing the flow of data as it was transferred to the computer for the drop test experiment. [21] (PowerPoint Clip Art, computer image) (circuitdiagram.org, coil-resistor schematic)

After collection, the data was postprocessed with code written in Python to find the velocity and voltage of each drop for the individual resistive loads. The individual drop data sets were extracted by finding the points at which the voltage spiked from the magnet moving through the coil. Figure 2.6 shows the data collected for one of the drops. Using the time values of the maximum and minimum voltage, a fixed amount of 0.01 seconds before the maximum voltage and after the minimum voltage was used to define the total time window for a given drop test. The same range of time was used to extract the velocity data corresponding to that drop.

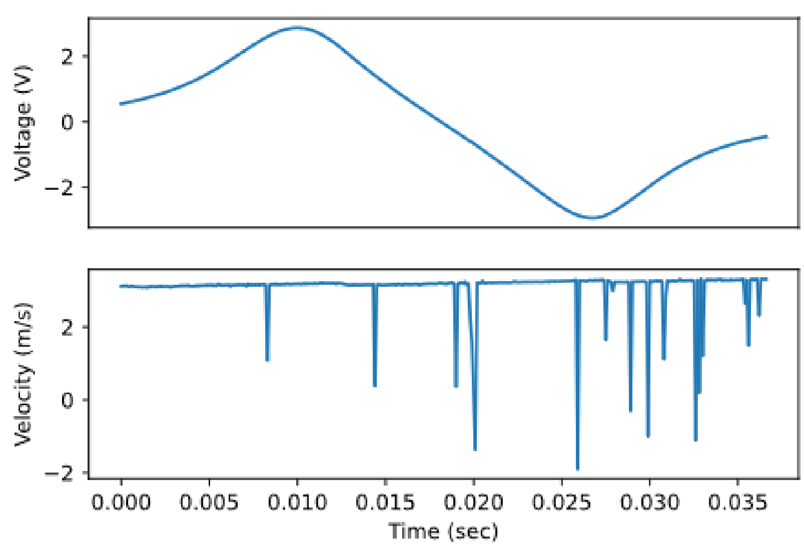

Figure 2.6. Voltage and velocity data for one drop test of the 10 MOhm resistive load experiment.

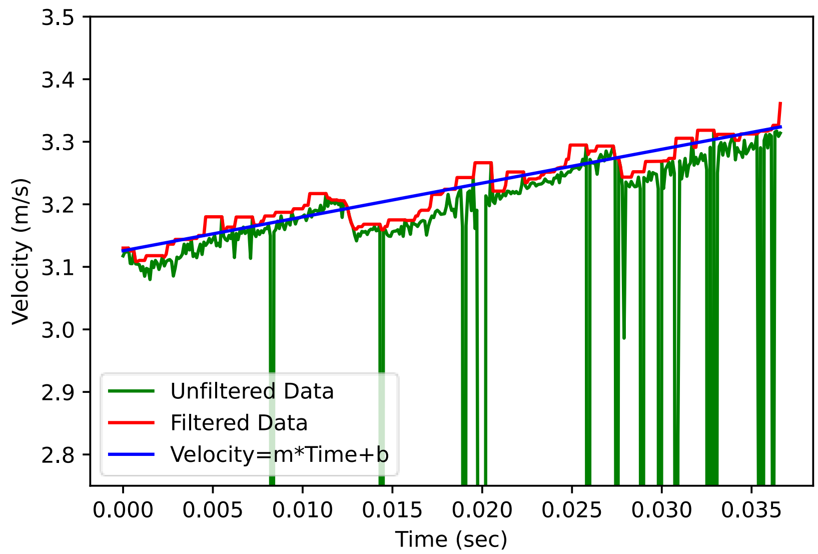

Figure 2.7. Postprocessing stages of the drop test velocity data.

After observing the extracted data in Figure 2.6, the velocity data was shown to be erratic in the sense that it dropped in value randomly throughout the measurement. This occurred because the vibrometer is designed to measure linear oscillations rather than just linear motion in one direction. With this, it was decided that it was an unreliable method for observing change in the velocity that could be used to calculate the force opposing the magnet motion. Even though the force was not calculated with the velocity data, the data was still used to find a comparison of the generated power. Ignoring the random jumps, a line of velocity data was found. Shown in Figure 2.7, a max filter with a window length of 10 samples was applied to the data. Then, a line of best fit in the slope-intercept form was fit to the filtered velocity values using the Python polyfit function. The average of the best fit for the time range set by the voltage was considered as the velocity in the center of the coil for that drop. The five drop tests with the smallest sum of squares error (SSE) between the line of best fit and the filtered data were selected to average their values for velocity and root mean square (RMS) voltage, V_{RMS}, to use with simulating and comparing the data. The SSE was calculated with

$$SSE = \sum_{i=0}^{n} [(Filtered\ Data)_i - (Best\ Fit\ Data)_i]^2 \quad (2.1)$$

where i is the position of each value of the two sets of velocity data to n. The root mean square, x_{RMS}, was statistically calculated to get an average specific to the voltage spike that could be compared with simulation using the equation,

$$x_{RMS} = \sqrt{\frac{x_1^2 + x_2^2 + \cdots + x_n^2}{n}} \quad (2.2)$$

where x_i are the values of each data point in the signal and n is the total number of points.

2.3 Finite Element Analysis of the Drop Test Experiment

FEA is applicable to many different areas of 3D simulation, with each area being unique in how they are modeled. This section will serve as a guide on how the electromagnetic simulations were modeled in this study by using the drop test simulation as a method for description.

2.3.1 Air Modeling

Electromagnetic fields are present everywhere, even in the vacuum of space. This means that the air must be modelled in electronics simulated in FEA to generate a clear picture of the electromagnetic fields interacting in them. After modeling the electronics, the first step in modeling this air is to create a box around all the electronics whose edges are far enough away from them so that the magnetic fields diminish to near zero values compared to the fields next to the components. The air box used for this simulation consisted of a box with 0.3048 by 0.3048 by 0.5334 m sides as shown in Figure 2.8.

After this, smaller air geometries around the electronics can be added whose mesh could be refined to improve the values of the simulation. None were added for this simulation, but the concept was used in Chapter 3. For simulations with motion like this experiment, a band must enclose the moving parts of the system for their entire range of motion. The band is used for defining the motion space of the moving parts that will be re-meshed at each time step in the FEA software. The band in this model was a cylinder of height 0.508 m and diameter of 0.04249 m, where the band diameter was the same as the inner diameter of the coil. It is important that the band does not touch the outside of the air box, so this band was centered vertically in it. When these parts are modeled, the necessary cavities are defined in each air component to rid the assembly of interferences which goes for the magnet and the band as well.

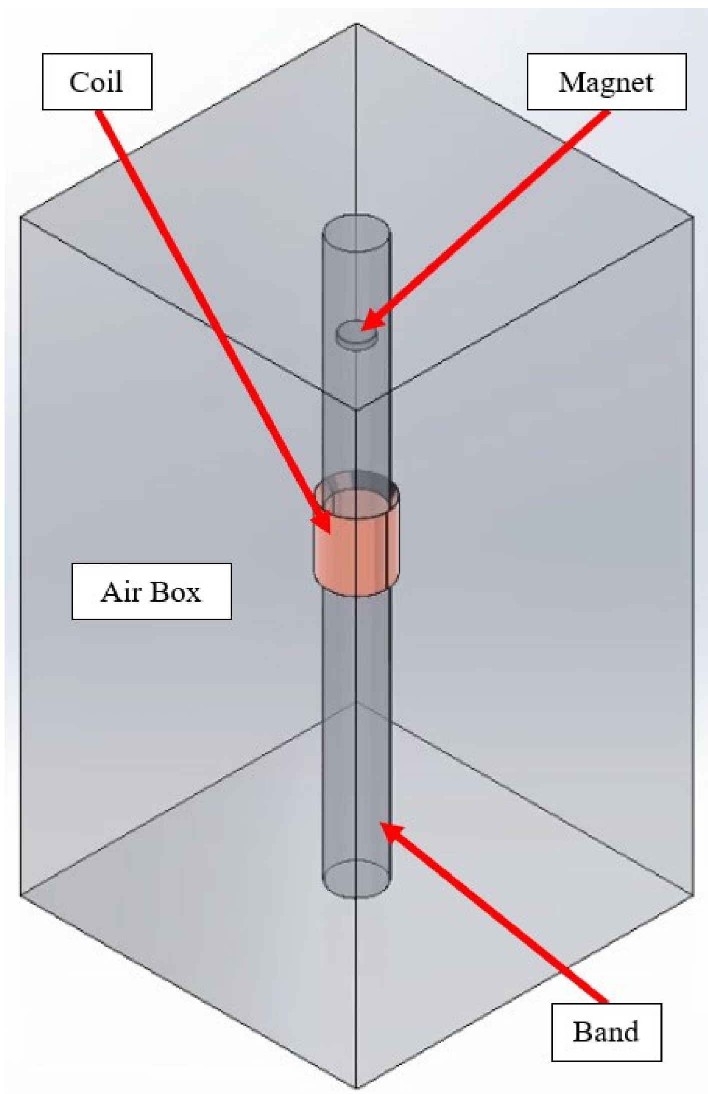

Figure 2.8. View of the air components (transparent) surrounding the magnet and coil.

2.3.2 Motion Modeling

Next, the movement is simulated using SolidWorks motion analysis. For this motion, the magnet was modeled as having a constant acceleration as it fell through the coil meaning the electromagnetic force acting on the magnet had no effect on the magnet motion. Using kinematics, the value for acceleration, a, was calculated with

$$v_f^2 = v_i^2 + 2a\Delta x \tag{2.3}$$

where v_f is the average velocity of the magnet in the middle of the coil as found in Section 2.2.2, v_i is the initial magnet velocity, and Δx is the total change in displacement. For calculating the acceleration, the length of the drop was estimated to be the length that the magnet fell through the guide, 0.6096 m, plus half the tallest height of the coil, 0.03048 m, for a total of 0.6401 m. Equation (2.3) was used to not only calculate acceleration of the magnet, but the velocity of the magnet 0.2032 m above the middle of the coil. This second calculation was made to cut down on simulation time by starting the magnet closer to the coil. Table 2.1 displays the calculated values for the acceleration and the velocity at 0.2032 m above the coil center to be used in the simulations for each resistance set collected. Setting the initial position of the bottom of the magnet 0.2032 m from the center of the coil, the initial velocity equal to the calculated velocity at the initial position, and the gravitational acceleration to the calculated acceleration in the software, the experimental motion was similarly modeled. The frames/s setting of the motion is used to determine the time steps at which the motion and FEA values are calculated in the simulation. For this model, the frames/s setting was set to 1000 which allowed for the values 0.01 seconds before the first extremum and after the last extremum to be used to calculate RMS voltage so the simulated data could be processed like the experimental data.

Table 2.1. Acceleration and velocity 0.2032 m from the center of the coil values used in the FEA simulation calculated with the collected velocity in the middle of the coil from each set of drops in the resistance sweep.

Resistive Load, Nominal (Measured)	Velocity in Middle of Coil (m/s)	Acceleration (m/s^2)	Velocity at 0.2032 m (m/s)
1 (1.0) Ω	3.12	7.59	2.58
10 (10.1) Ω	3.14	7.72	2.74
100 (99.8) Ω	3.13	7.67	2.73
1 (0.994) kΩ	3.22	8.12	2.81
10 (9.99) kΩ	3.20	8.01	2.80
100 (100.7) kΩ	3.14	7.70	2.74
1 (0.996) MΩ	3.27	8.38	2.86
10 (9.98) MΩ	3.20	8.00	2.79

2.3.3 Electromagnetic Simulation

With the motion defined, the FEA software was then implemented. First, the transient magnetic study was created with the motion coupled to the system along with the band and magnet designated as the band and the moving parts, respectively. The next step was to define the materials of the components. The air parts, including the band, were set to the air material while the coil component was set to copper. For the magnet, the BH curve had to be defined. The BH curve describes the magnetic properties of a permanent magnet [22]. The way the magnet interacts with the environment it is in is dependent upon this curve. Displayed in Figure 2.9, BH curves of permanent magnets consist of positive magnetic flux values in units of Gauss, B, and negative applied magnetic field values in units of Oersted, H. The load line, or permeance coefficient, that determines the operating point along the BH curve is the ratio between B and H. FEA numerically calculates this operating point to determine how the magnetic flux of the permanent magnet acts when it is subjected to other magnetic fields. As the magnet moves, the operating point changed which made FEA a great resource for solving this model as it could recalculate it at every time step.

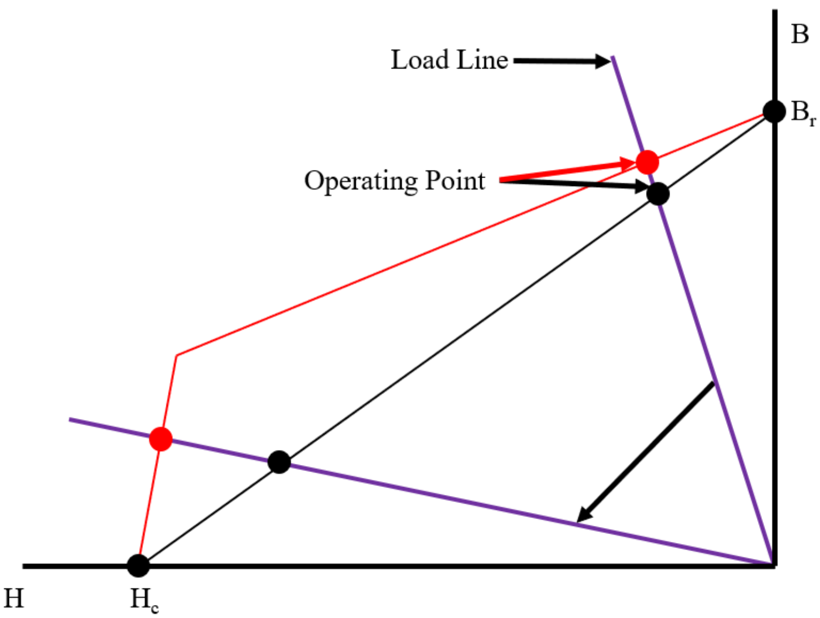

Figure 2.9. The BH curve of a magnetic material for a linear (black) and nonlinear (red) curve along with the respective operating points along the moving load line. This plot is to display the differences between the curves but holds no numerical significance.

For N52 magnets, the relationship between B and H is nonlinear as depicted in Figure 2.9. Set values of B along H were documented for the magnet and attempts were made to use these values directly with the software. After these efforts, it was discovered it took large amounts of simulation time to implement this curve that inevitably would have made FEA impractical. With advice from the software company, the BH curve was modeled as linear with the axis intercepts set as the remanence, B_r, and the coercive force, H_c. These values were all that were needed by the software to define the permanent magnet properties in the linear model.

Although this simplification will lead to inherent errors, the software company stated that the error would be small enough that they will not skew the final values too far from the actual values calculated with a nonlinear simulation. Along with the BH curve, the documentation of the magnets also gave a range for remanence, 14500-14800 Gauss, and a minimum for coercive force, 12000 Oersted, that were used to set the final properties for modeling the magnet, 14800 Gauss and 14000 Oersted, respectively [23]. The last step for defining the magnet was to set its coercivity direction, or magnetization direction. The magnet was axially magnetized with a direction set to point down along the direction of motion.

With all the materials set, a wound coil was defined with the coil components selected as the entities. The coil was split into two halves to expose a face in the part that would sever the wires and make them accessible as shown in Figure 2.10. With it split into two parts, one of the faces was selected to be the entry and exit port for implementation in the virtual circuit case. The software allows the wire gauge, wire diameter, or filling factor and the number of turns to be defined for the coil. For this experiment, a wire gauge of 22 AWG was documented so it was used to define the coil along with 500 turns. The final step before running the simulation was to define the circuit case. Figure 2.11 shows the circuit case assigned with the coil and resistive load, R_L, in series along with the required ground.

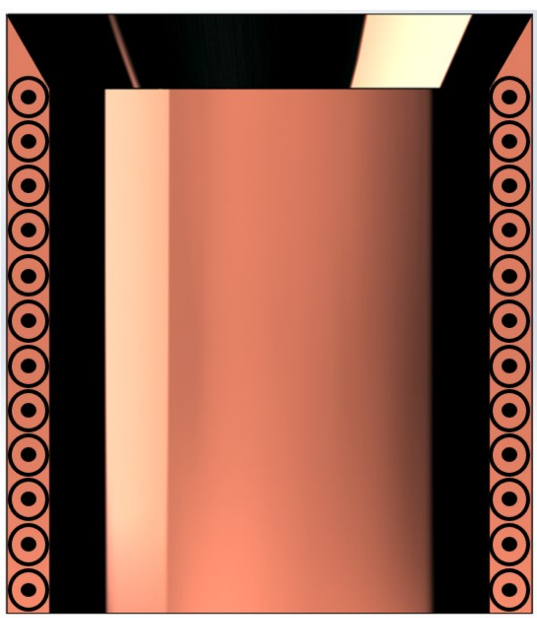

Figure 2.10. Cross section of the coil displaying how it needed to be split to expose the face where the wires would be severed.

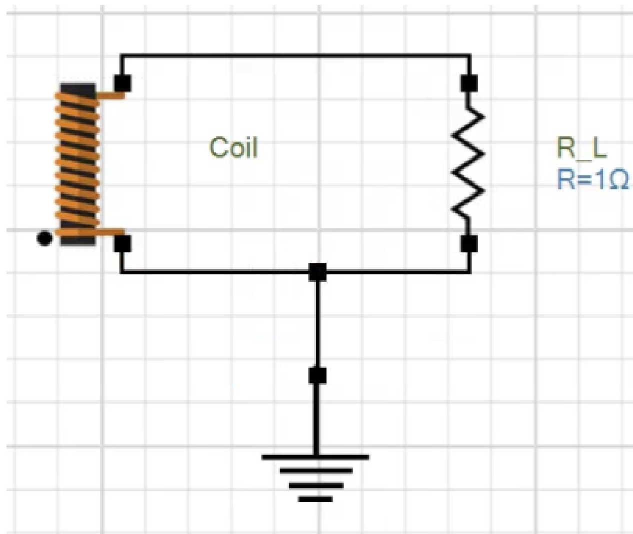

Figure 2.11. Circuit case assigned in the FEA simulation of the 1 Ohm drop with the resistive load and coil in series.

After the simulation was built and could be executed, mesh controls were applied to see the different effects on the value of interest, V_{RMS}. There was no calculation of the voltage in the resistor provided so the simulated current in the coil was used to calculate the voltage across the different resistive loads since the current in a series circuit is uniform. The calculation used was Ohm's Law,

$$V_L = I_c R_L \tag{2.4}$$

where I_c is the current in the coil (A), R_L is the resistive load (Ω), and V_L is the voltage across the resistor. The software gave options to apply mesh controls to the surfaces and the volume of parts. The final accepted controls used were surface meshes on all surfaces of the magnet of size 2.108 mm and a surface mesh on the coil surfaces of size 1.905 mm. The global mesh, which mainly controlled the air parts, was kept at the original settings of 27.43 mm because it had minimal effect on the value in question. Table 2.2 shows the calculated V_{RMS} of the accepted mesh of one of the drop test experiments along with a mesh that halved the accepted surface controls and the volume mesh of the air components and a mesh with volume controls of half the surface element size. The percent change, PC, was calculated using

$$PC = \frac{x_{sim2} - x_{sim1}}{x_{sim1}} * 100\% \tag{2.5}$$

where x_{sim2} were the values calculated with the more refined meshes and x_{sim1} were the values of the accepted mesh used for the final results comparison to show that refinement had very small effect on V_{RMS}.

Table 2.2. The RMS voltage percent changes of two different mesh refinements from the accepted mesh. SM indicates a surface mesh was applied and VM indicates a volume mesh was applied.

Mesh Indication	Mesh Control Size (mm)			V_{RMS} (V)	Percent Change from Accepted Mesh (%)
	Magnet	Coil	Global		
Accepted	2.108 (SM)	1.905 (SM)	27.43 (VM)	1.726	-
Surface Halved with Air	1.054 (SM)	0.953 (SM)	13.72 (VM)	1.727	0.05
Volume Halved	1.054 (VM)	0.953 (VM)	27.43 (VM)	1.728	0.12

2.4 Experimental and Simulated Results of the Drop Test Experiment

After the simulations for each resistive load were run, a comparison was made between the experimental and FEA results for both RMS voltage and power, P_{RMS}. P_{RMS} was calculated using the equation for electrical power

$$P_{RMS} = \frac{V_{RMS}^2}{R_L}. \tag{2.6}$$

After calculating these values, the percent differences between the simulated and experimental data were found for comparison. The percent difference, PD, was calculated using

$$PD = \frac{x_{sim} - x_{exp}}{x_{exp}} * 100\% \tag{2.7}$$

where x_{sim} is the simulated value and x_{exp} is the experimental value. Looking at Table 2.3 and Table 2.4, there was good agreement between the values. By finding the right magnet properties of remanence and coercive force, the values for voltage all fell within 10% of each other while the power comparison yielded a maximum percent difference of 15.52%. Overall, this experiment showed good agreement in the electrical values and gave reason to move forward with the finite element model although an electromagnetic force comparison could not be attained. After seeing where the drop test experiment fell short, it was decided that a new method was needed for collecting this force measurement.

Table 2.3. RMS voltage comparison of the experimental and simulated results.

Nominal Resistance Load	Exp RMS Voltage (V)	FEA RMS Voltage (V)	Percent Difference (%)
1 Ω	0.35	0.32	-8.09
10 Ω	1.26	1.22	-3.59
100 Ω	1.69	1.66	-1.75
1 kΩ	1.78	1.72	-3.29
10 kΩ	1.78	1.74	-2.01
100 kΩ	1.75	1.70	-2.55
1 MΩ	1.81	1.69	-6.68
10 MΩ	1.78	1.73	-3.00

Table 2.4. RMS power comparison of the experimental and simulated results.

Nominal Resistance Load	Exp RMS Power (W)	FEA RMS Power (W)	Percent Difference (%)
1 Ω	1.22E-01	1.03E-01	-15.52
10 Ω	1.58E-01	1.47E-01	-7.05
100 Ω	2.85E-02	2.75E-02	-3.47
1 kΩ	3.18E-03	2.97E-03	-6.48
10 kΩ	3.15E-04	3.03E-04	-3.98
100 kΩ	3.03E-05	2.87E-05	-5.04
1 MΩ	3.28E-06	2.86E-06	-12.92
10 MΩ	3.20E-07	3.01E-07	-5.91

2.5 Summary and Conclusions

This chapter presented the methodology behind creating experimentally validated finite element models as well as introduced the electromagnetic simulation software by explaining how it works along with an experiment. The basis of validation for this study was to produce measurable values for electromagnetic force and electrical power generated by a known relative motion of a magnet through a coil. With these three values, the FEA software could be used to model it to validate its use in characterizing the relationship between the properties under inspection. The first attempt at measuring these values was a drop test experiment.

The drop test aimed to excite a voltage in a coil by dropping a magnet through it to generate an electromagnetic field that would oppose the permanent magnetic field, thus slowing down the magnet and providing a way to calculate the opposing force from the motion data. The experiment utilized a DAQ to collect the velocity data from the vibrometer and voltage across different resistive loads. It was discovered that the vibrometer was not capable of accurately measuring the velocity in this configuration. Although the force could not be calculated using the change in velocity, the velocity moving through the coil could still be estimated. Using this estimation, a finite element model of the drop test was made.

The chapter details how the simulation software models the air and electronic parts, motion, magnets, coils, and circuit cases. Along with the modeling, the mesh controls available in the software are discussed along with how the voltage across the resistive load was calculated using the coil current. Through this modeling, voltage and power comparisons were made.

The comparisons between the experimental and simulated results yielded promising agreement between the voltage and power as the maximum magnitudes of percent difference were 8.09% and 15.52%, respectively. These results gave reason to continue working with the software. It was decided after this experiment, a more controlled system was needed to measure the electromagnetic force of a coil opposing the motion of a magnet.

Chapter 3

Final Experiment and Validation of the Finite Element Model

3.1 Shaker Table Experiment

After the early work discussed in Chapter 2, it was determined to ensure the experiment would provide a measurable electromagnetic force acting against the motion of the system, the motion had to be controlled externally while the force was measured directly. An electrodynamic shaker table (Labworks 127.123-500D12 DuoBase System) was employed to dictate the system motion as force and voltage measurements were recorded. The benefit of using a shaker table was it could generate oscillatory sine motion which imitated the actual movement of a linear alternator. This motion resulted in periodic voltage and force with frequency domain content that changed based on the geometry and relative displacement of the magnet and coil. This section details the experimental methods used to validate the ability of FEA to predict the electrical power and electromagnetic force generated in a linear alternator according to different resistive loads.

3.1.1 Designing a Fixture to Increase Peak-to-Peak Displacement of Motion

For this experiment, a design which permitted the magnet to fully exit the coil while oscillating was desired. This allowed for the observation of how the magnet-to-coil length ratio and peak-to-peak displacement affected the force and voltage results. Figure 3.1 defines dimensions used for the magnet and coil length and the oscillation of the magnet relative to the coil. The shaker table had a maximum peak-to-peak displacement of 2.54-cm. Since the disc magnets available for use in the experiment had a maximum length of 2.54-cm, the larger magnets could not completely exit a coil that matches or is larger in length at any point in the motion. This caused a problem as the experiment needed to be adaptable so different lengths of coils and magnets could be installed until a measurable force was collected. In order to solve this problem, a fixture was built that increased the maximum peak-to-peak displacement of the motion to ensure that the larger magnets could be used in the experiment.

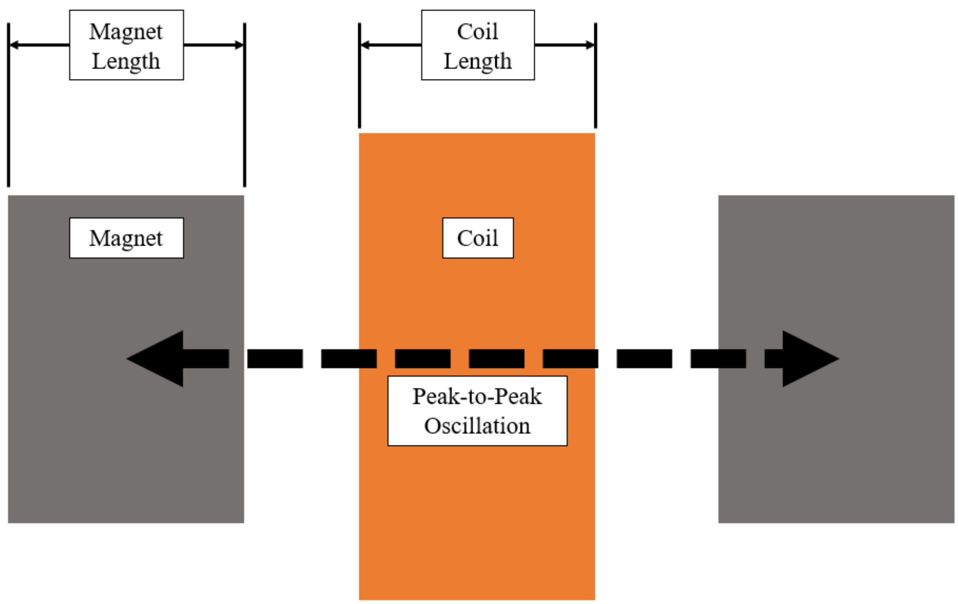

Figure 3.1. Diagram of the dimensions used to define the magnet-to-coil length ratio and the peak-to-peak displacement of the magnet oscillation relative to the coil.

The fixture utilized the classic 1 degree of freedom (DOF) base excitation model to increase the maximum displacement. This mathematical model is used to calculate the equation of motion for a mass-spring system on a base excited with harmonic motion, $y(t)$, as shown in Figure 3.2 [24]. This base excitation causes the mass to oscillate at the same rate as the harmonic frequency in Hz, f_H, with the mass motion denoted as $x(t)$. For the mass-spring system, the natural frequency in Hz, f_n, is solved for using

$$f_n = \frac{1}{2\pi}\sqrt{\frac{k_{eff}}{m_{eff}}} \tag{3.1}$$

with k_{eff} being the effective spring constant and m_{eff} being the effective mass. As f_H approaches f_n, the ratio of the mass oscillation amplitude, A_m, and the base excitation amplitude, A_s, also known as displacement transmissibility, can become quite large dependent upon the damping coefficient, c. This model was used to design a mass-spring fixture with a natural frequency that could be excited by the shaker table.

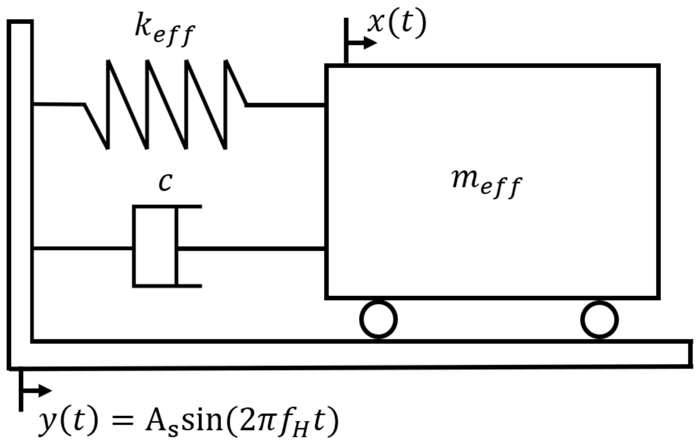

Figure 3.2. Depiction of a mass-spring system base excitation model with 1 DOF.

Figure 3.3 shows the fixture built that consisted of two sets of extension springs connected to opposite sides of a linear bearing carriage (THK Model HSR20LR). With no intentionally applied damping forces, the displacement transmissibility was as large as the physical system would allow. Each set of springs were preloaded to half their documented maximum load length to give the carriage the maximum range of oscillation displacement the springs could provide. In the initial stages of the design, it was decided that the magnet was easier to couple to a force sensor than the coil for the electromagnetic force measurements, so the coil was used as the mover in the experiment. The carriage was equipped to hold the coil in a 3D printed clamp while translating along a guide rail. Using a mass-spring system allowed for a streamlined approach to estimate the natural frequency of the carriage by supplying a documented spring constant. A spring was found that allowed for a peak-to-peak displacement near 5.08-cm. This would permit the 2.54-cm-long magnet to fully exit a 2.54-cm-long coil during oscillation, thus satisfying the design objective. The final springs used were steel extension springs (McMaster-Carr PN 9654K826) with a minimum length of 12.7-cm and a maximum length of 17.78-cm along with a nominal spring constant, $k = 14010$ N/m.

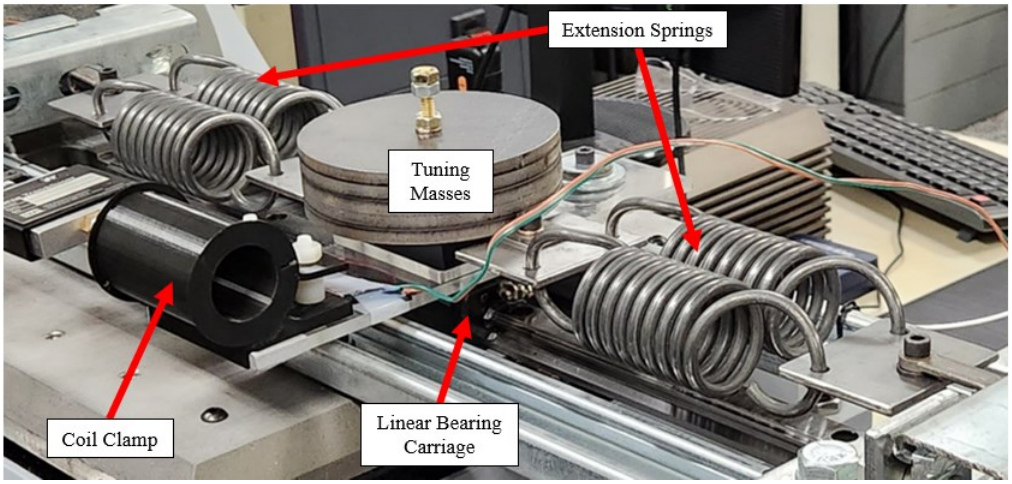

Figure 3.3. Photo of the shaker table experiment and fixture used for increasing the maximum peak-to-peak displacement of the coil beyond that of the shaker table.

After finding a spring with the desired maximum displacement and stiffness, the estimated carriage mass was needed to find f_n. Due to concerns of unwanted magnetic forces and eddy currents being generated in the steel of the carriage and the guide rail, a piece of 0.635-cm-thick by 7.62-cm-wide acrylic was used to extend the closest edge of the coil 7.62-cm away from the carriage. The clamp holding it was tightened down to the acrylic with plastic screws to keep the area free of metal as well.

A 1.27-cm-thick piece of Delrin was cut to the size of the rectangular top face of the carriage and a countersunk hole was bored in the middle of it allowing a screw to protrude to attach an arm for the springs to hold on to and allow additional mass to be added to the system as needed for natural frequency tuning. The two pieces of acrylic and Delrin were then bored to fit the holes on the carriage and fastened to it using its threaded holes. When the initial carriage design was complete, its total mass was estimated so the natural frequency could be calculated using equation (3.1).

As expected, aspects of the carriage were changed during the build process, so the final measured mass was larger than the estimated mass. For the following calculations to show how the natural frequency was estimated, the effective mass as observed from the natural frequency tuning method was used, 2.46 kg. This tuning was done by observing the free vibration of the carriage as mass was added to it while collecting its oscillation velocity from the vibrometer used in Chapter 2 and shown in Figure 3.4. LabView was used to calculate and display the power spectral density (PSD) of the velocity response to approximate the first natural frequency which then was used with the effective stiffness of the springs to calculate the mass. For the configuration of the carriage with two extension springs on each side, the effective stiffness was calculated using

$$k_{eff} = 4k \tag{3.2}$$

with the spring constants being added together because they are in parallel. Using the nominal spring constant for k to estimate the natural frequency of the system, the effective stiffness for this system was 56040 N/m which when used with the effective mass in equation (3.1) yields the operating frequency of the experiment, 24 Hz.

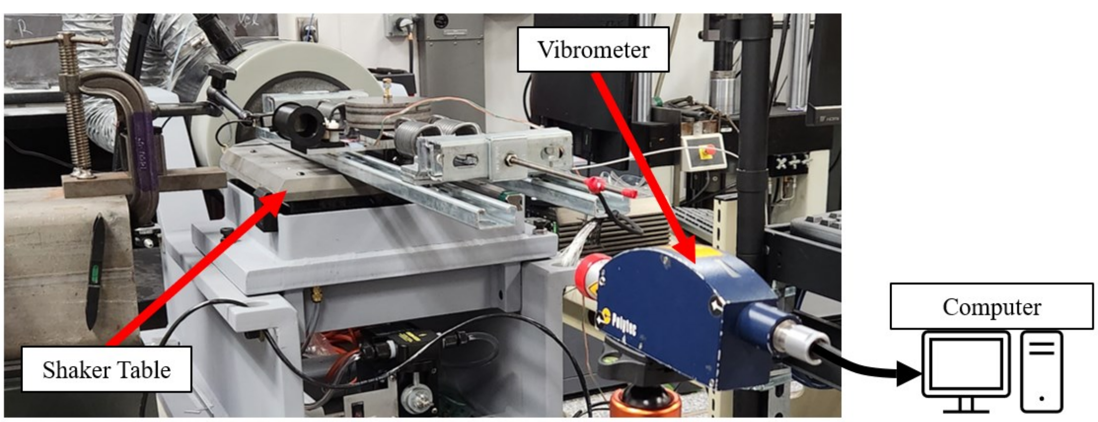

Figure 3.4. Photo of the vibrometer in relation to the shaker table for measuring the motion of the carriage. (PowerPoint Clip Art, computer image)

3.1.2 Electromagnetic Force Measurement

This experiment utilized a 2.2 lbf (10 N) capacity load cell (MTS Model 661 09A-20) to measure the electromagnetic force generated in the system. Any added vibration from the supporting structure could have affected the final signal collected by the load cell, so the load cell support structure, displayed in Figure 3.5 (A), consisted of a weighted down table to reduce vibration propagation in it coming from the running shaker table and the force acting on the load cell. The load cell position was manipulated with an adjustable holding arm (NOGA MG10533), shown in Figure 3.5 (B). This arm was used to align the magnet within the coil both axially and angularly for the experiments.

(A)
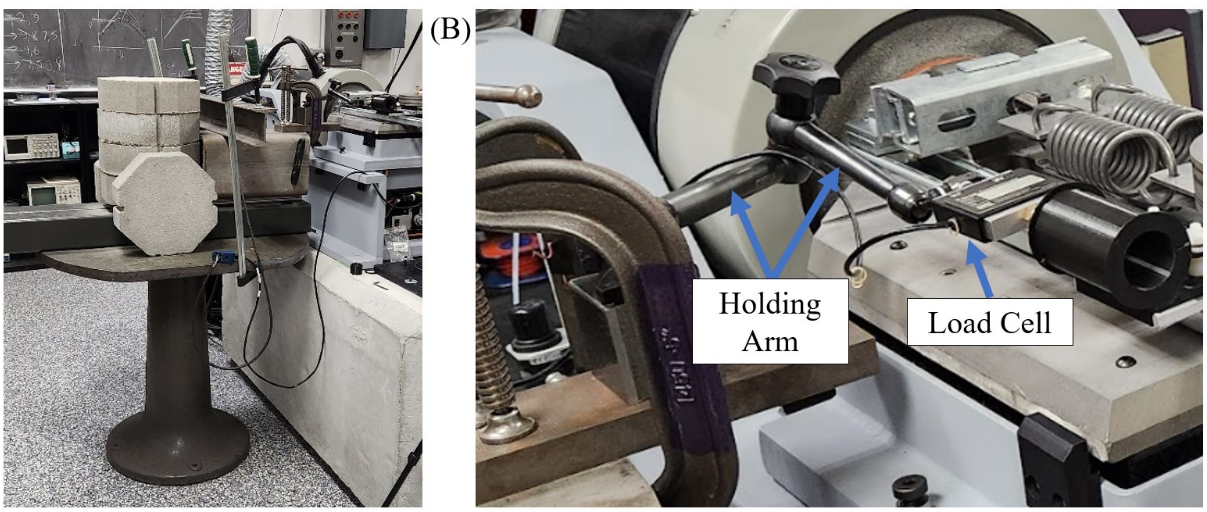

Figure 3.5. Load cell supporting structure. (A) Weighted down table. (B) Holding arm for aligning the load cell within the coil.

The thread size of the load cell anchoring hole was 1/4"-28, so the attraction of a Grade 8 1/4"-28 threaded screw to the magnet was used to fix the magnet in place as shown in Figure 3.6 (A). The effects on the magnetic field from the steel screw and any eddy currents generated in it were assumed to be negligible. Also shown in Figure 3.6 (B) are the two 3D printed sleeves designed to center the screw, magnet, and coil in relation to one another. The magnet sleeve first had the screw inserted through a hole in the surface facing the threads of the screw. Then, the magnet was slid over the top of the screw and centered on the axis of it, and the load cell because the magnet sleeve had the same 2.54-cm inner diameter as the magnet. After this, the coil sleeve was inserted inside the coil housing and the magnet was guided into place with small protrusions on the magnet sleeve that fit the guide slits of the coil sleeve. The magnet was inserted as far as needed for it to be axially centered within the coil length. Figure 3.7 shows the load cell coupled to the magnet with it properly aligned in the coil.

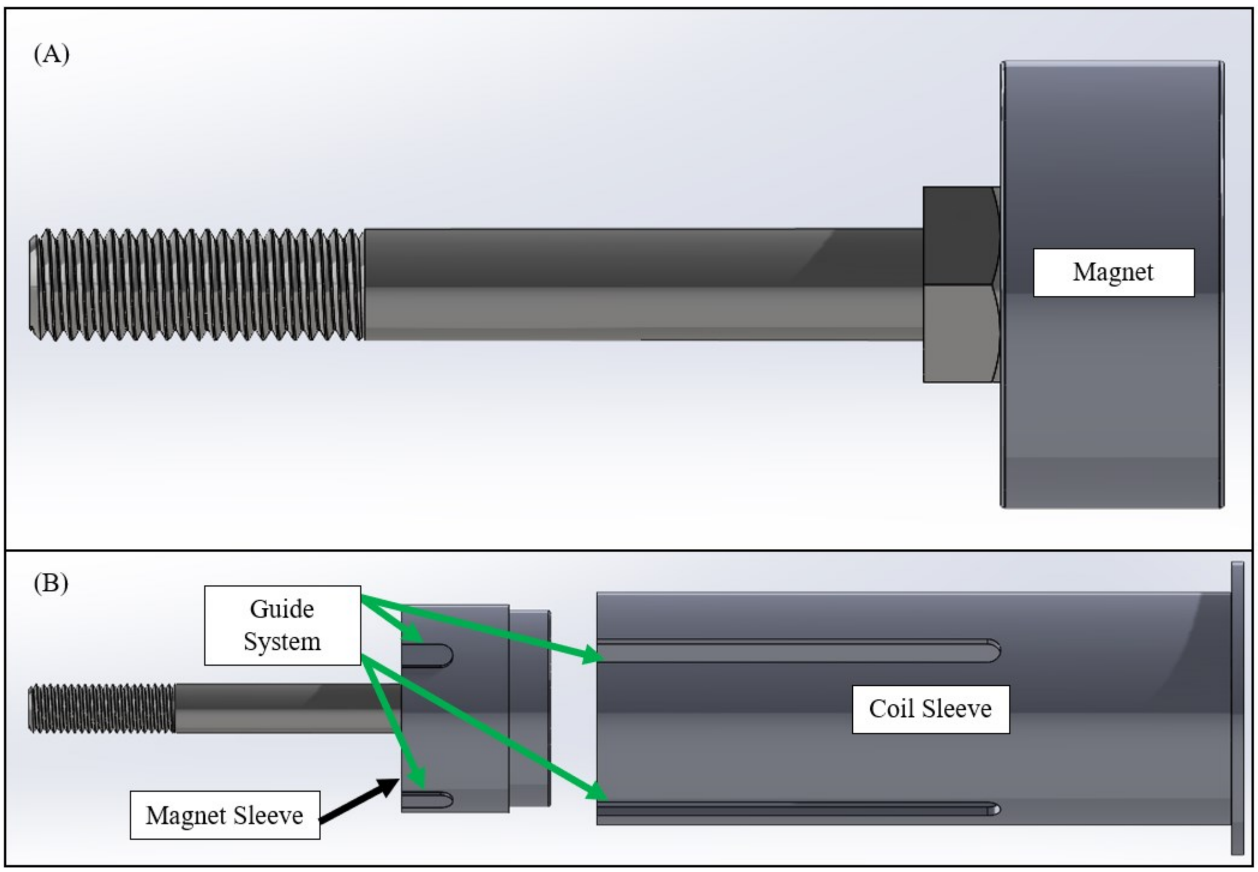

Figure 3.6. (A) Magnet configuration in relation to the screw used to couple it to the load cell. (B) Magnet sleeve and coil sleeve for aligning the magnet in relation to the screw and coil, respectively.

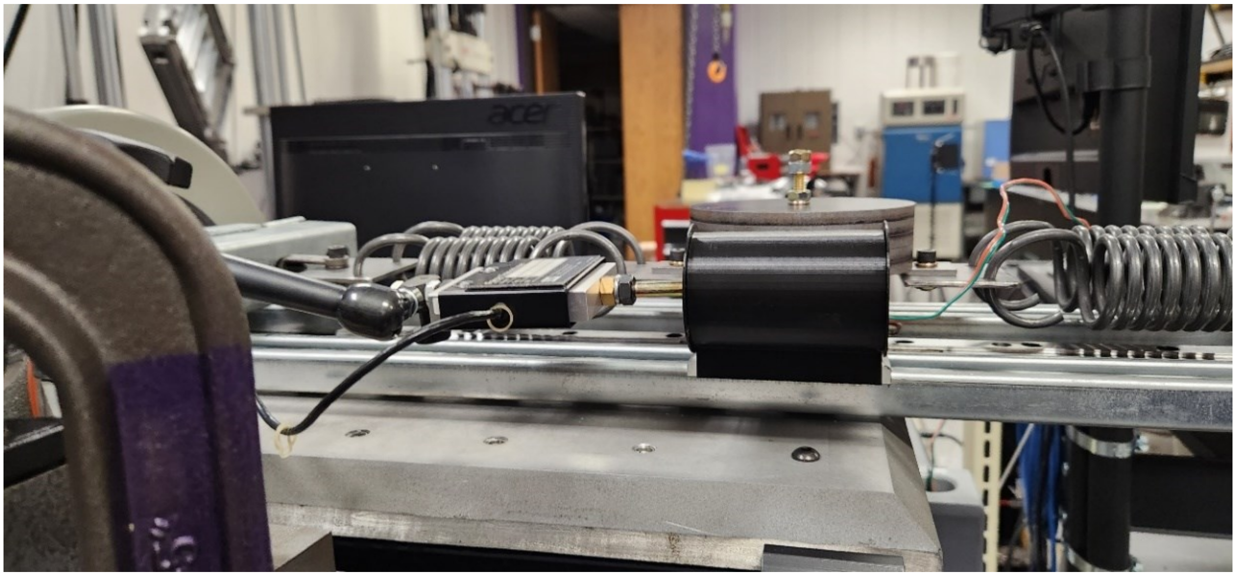
Figure 3.7. The load cell ready for operation with the coupled magnet aligned with the coil.

3.1.3 Data Collection

The final experiment used an N52 disc magnet with a length of 1.27-cm and diameter of 2.54-cm. The 1.27-cm-long magnet was chosen because it provided the strongest magnetic field of the permanent magnets available that could exit and travel outside of a coil of equal length with the maximum possible displacement. The coil used was wound the same way as described in Chapter 2 but with only 250 turns of 30-gauge enameled magnet wire with a coil length of 1.27-cm. These dimensions made the magnet-to-coil length ratio 1:1. The inner diameter of the coil was 3.366-cm with an outer diameter of 3.649-cm measured after winding was complete.

Three measurements were recorded with LabVIEW and processed to validate the simulation results: electromagnetic force acting on the magnet, coil velocity, and coil voltage across a resistive load. Unlike the voltages of the vibrometer and coil that could be measured using the analog input channel of most DAQs, the load cell required a bridge module to process the voltage output for force measurement. A cDAQ-9174 4-module chassis was employed for its ability to measure both types of inputs at the same time. The chassis controls the timing, synchronization, and data transfer between NI C Series I/O modules to the computer [21]. The two modules used for this experiment were the NI-9205 for analog voltage measurement and the NI-9237 simultaneous bridge module for force measurement. Figure 3.8 displays the diagram for all three measurements collected by the cDAQ and how the data was transferred to the computer. Using the NI-9205 as a full bridge, the force measurement was converted within LabView to Newtons and saved as such after static calibration of the load cell.

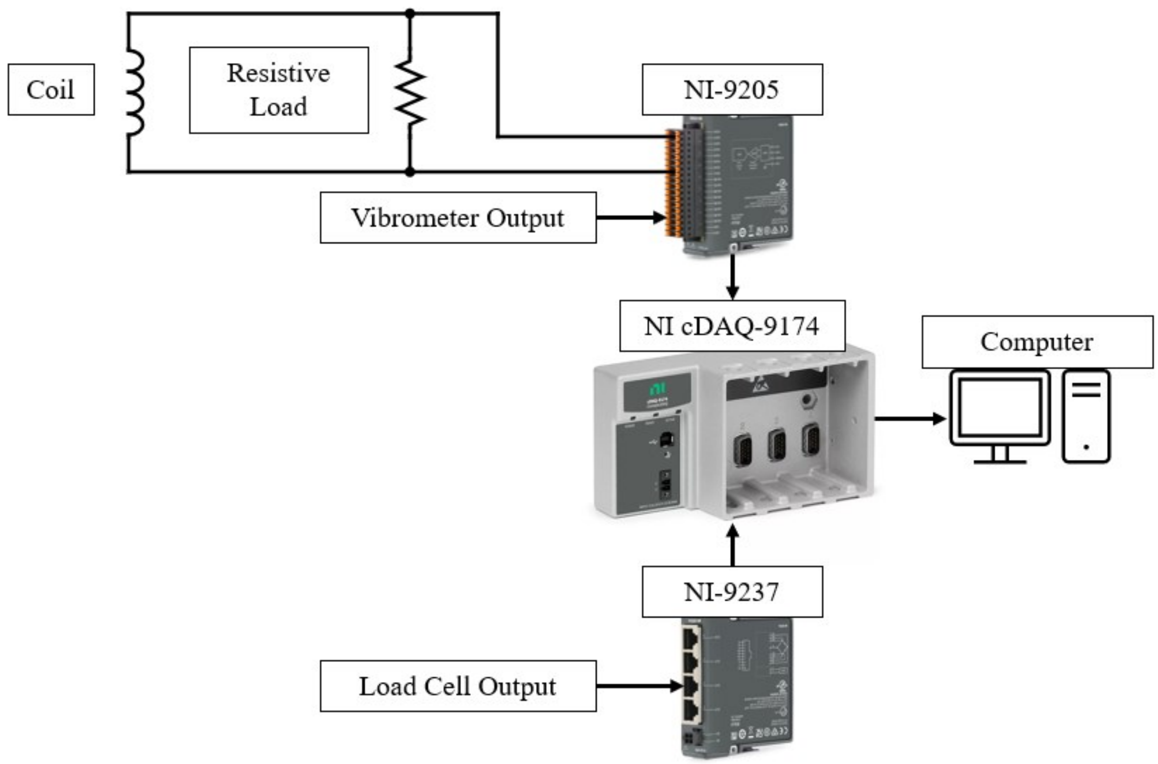

Figure 3.8. Diagram showing the flow of data through the electronics to the computer for the shaker table experiment [21]. (PowerPoint Clip Art, computer image) (circuitdiagram.org, coil-resistor schematic)

The NI-9237 was used to collect both the vibrometer and coil voltages. The vibrometer measured the carriage velocity by placing it parallel to the motion of the cart and pointing the laser at a piece of reflective tape attached to the acrylic beam holding the coil. The internal fast-tracking filter was used with the vibrometer to improve signal quality. A display was made in

LabView that showed the real-time velocity and displacement of the carriage during operation to monitor coil motion as shown in Appendix C. The steady state peak-to-peak displacement, A_{pp}, was calculated using

$$A_{pp} = 2 * \frac{V_p}{2\pi f_m} \tag{3.3}$$

where f_m is the measured excitation frequency and V_p is the peak velocity.

Five peak-to-peak displacements were chosen as the operating points of data collection ranging most of the available maximum displacement. These displacements were 0.69, 1.52, 2.34, 3.30, and 4.24-cm. The reason the maximum displacement of 4.24-cm was chosen and not 5.08-cm was to ensure that no springs would fully close. The frequency of the shaker table motion was set to the natural frequency of the carriage, 24 Hz, and its own displacement was increased until the carriage reached each operating displacement point. The coil voltage was measured across a nominal resistive load decade sweep from 1 Ohm to 1 MOhm and included an open circuit case to define the noise floor of each operating displacement. This resulted in eight sets of data for each displacement up to 3.30-cm. The only values collected for the 4.24-cm displacement were the noise floor, 1 Ohm, and 10 Ohm parts of the sweep.

Calculations were conducted before collection to ensure a sufficient amount of time series data was recorded for postprocessing. The frequency resolution of discrete Fourier transforms, such as the fast Fourier transform method used to calculate the spectral densities of data in Python, is dependent upon the amount of time series data points they are given [25]. These functions require three main arguments to calculate the power spectrum of a data sequence: time series signal, sampling rate, and number of segments for the frequency range. The frequency resolution, f_r, of the data was found with

$$f_r = \frac{f_s}{N} \tag{3.4}$$

where f_s is the sampling rate and N is the number of the segments that must be less than or equal to the number of data points provided. The number of segments was input into the Python frequency domain operations using the nperseg argument of the function. This value must be a power of 2 for fast Fourier transforms [25]. In order to record data in a reasonable amount of time with high resolution, equation (3.4) was employed to calculate the collection time needed for each configuration of the experiment. In the end, at least 66 seconds of data at a sample rate of 2000 Hz was collected, which yielded a sequence of at least 132,000 samples per experiment with 131,072 being the nearest lesser power of 2. Using this for nperseg gave a frequency resolution of 0.0153 Hz which was decided to be sufficient for quality frequency domain plotting and fitting (shown later).

3.2 Dynamic Calibration of Collected Force Signals

It is well-known that sensors often have dynamics that can cause signal attenuation during measurements. It was noticed early on that the load cell in this study used to measure the electromagnetic force acting on the magnet had dynamics that needed to be accounted for. Since the motion of the shaker table experiment was periodic, the force acting on the load cell was also. This periodic force excited the dynamics of the load cell, causing the output force signal to be distorted from the input force. Ewins (1995) exhibited a simple way to visualize the dynamics of a system by plotting its frequency response function, also known as its transfer function [26]. The transfer function, $H(s)$, is statistically calculated in the frequency domain, s, with the relation

$$H(s) = \frac{S_{xy}(s)}{S_{xx}(s)} \tag{3.5}$$

where $S_{xx}(s)$ is the auto spectra of the excitation signal, with the signal denoted as x, and $S_{xy}(s)$ is the cross spectrum between the response signal, y, and the excitation signal. Both the auto spectra and cross spectrum are correlation functions of their respective signals [26]. For later comparisons, the response will be referred to as the output and the excitation as the input. A common method for collecting this input and output data is exciting the device under test with an instrumented impact hammer.

3.2.1 Collection of the Transfer Function with the Impact Hammer Test

For this study, an impact hammer (PCB Piezotronics Model 086C01) was used to strike the magnet surface pointing away from the load cell while a sensor signal conditioner (PCB Piezotronics Model 482C) modified the hammer output so LabView could collect the time series force signal of the hammer. By striking the magnet surface pointing away from the loadcell an excitation from the same direction as the electromagnetic force the magnet experienced during the experiments was applied on it, thus exciting the same dynamics. Simultaneously, the load cell time series data was collected. For reasons explained later in this section, the magnet had to be struck while positioned within the coil. A rigid plastic tube was fixed to the end of the impact hammer so it could strike the magnet without creating magnetic forces on the hammer. A picture of the hammer with the extension tube is shown in Figure 3.9. The effects from the addition of the tube on the impact measurements were assumed to be negligible.

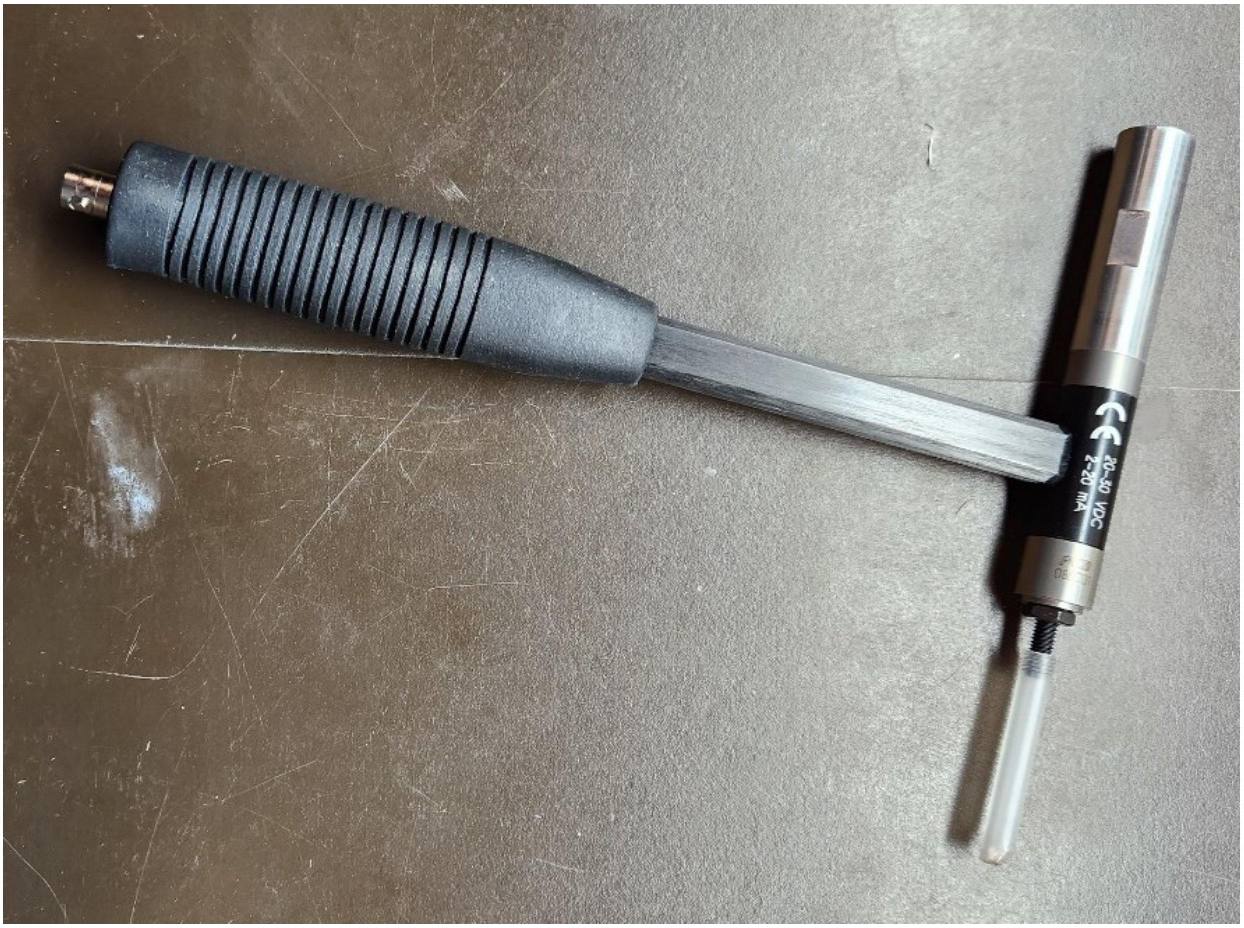

Figure 3.9. Impact hammer with tube fixed to its end to extend the striking reach.

In practice, an impact hammer is a load cell designed for striking structures to induce vibration. The ideal characteristic of an impact test is that the input magnitude of the power content is spread evenly across the hammer bandwidth (~1 kHz). By impacting the loadcell, the bandwidth of interest (200 Hz) was excited with equal power. This can be seen in plot (B) of Figure 3.10 with the effects the dynamics had on the output signal in plot (A). The cross spectrum and auto spectra of the tests were found using the Python signal.csd function. The input, x, was the hammer time series signal and the output, y, was the load cell signal. As seen in the following figures, the resulting transfer function for the two tests were similar in shape and magnitude because the output magnitude was directly proportional to the input magnitude.

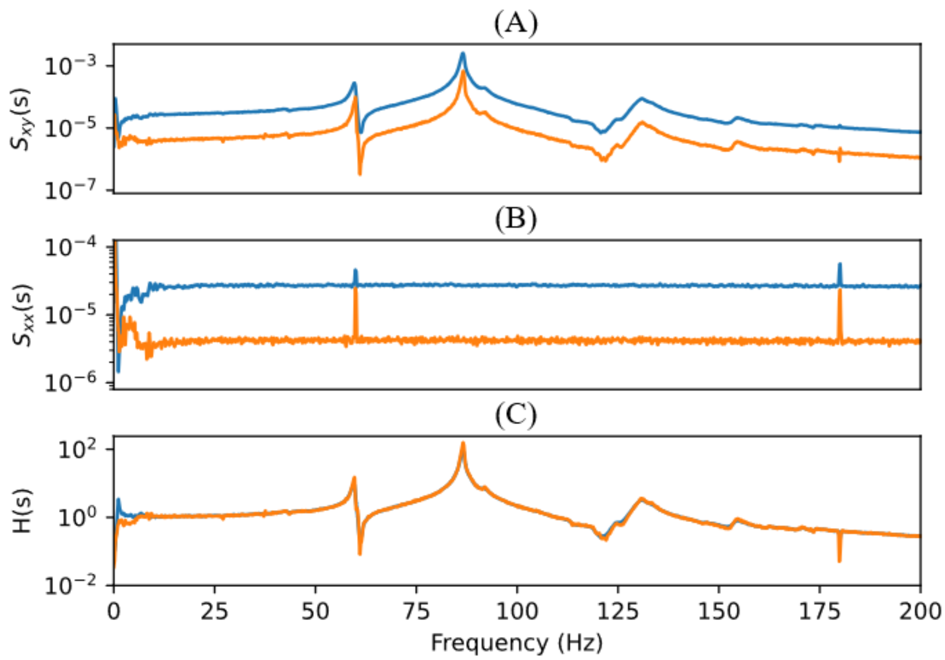

Figure 3.10. Processed results of two impact tests from the final experiment configuration, (A) The cross spectrum of the hammer and load cell signals. (B) The auto spectra of the hammer signal. (C) The calculated transfer function of the load cell for both tests.

Early attempts to characterize the dynamics involved a 100 N load cell (MTS Model 513406-03) and the 10 N load cell. An electromagnet was used to excite each load cell coupled to the permanent magnet with a sweeping periodic force from 10 to 200 Hz. The load cells were excited at separate times, each being situated in the same position in relation to the electromagnet for the respective tests. The same permanent magnet and screw were also used with both load cells. The electromagnet power was supplied by an amplifier output (Fosi Audio TB10D) of a sweep function generator signal (Krohn-Hite 1200). Like the impact hammer, the 100 N load cell output was to be used as the trusted signal for the input force from the electromagnet, assuming the force seen by the load cells did not change between tests. Due to the relation of the dynamics and the effective mass and spring constants, any change in mass coupled to the load cell or position of the structure holding it will affect the power content of the dynamics and the frequencies at which the system naturally vibrates. In the end, the impact hammer test provided the most consistent transfer function because the electromagnet test required the load cell and supporting structure be moved after data collection, thus altering the dynamics of the system.

The impact tests were run after the experiment was complete with the magnet still positioned in the coil to ensure the collected transfer function supplied the same dynamics as the system during the shaker table experiment. In total, six impact tests were conducted, processed as shown in Figure 3.10, and averaged to obtain the transfer function of the system, denoted as H_{IT}. A comparison of H_{IT} and the transfer function of the electromagnet test, H_{ET}, is displayed in Figure 3.11. Besides the obvious lower quality in H_{ET} compared to H_{TF}, this shows that there was a noticeable difference in the dynamics of the system past 120 Hz between the tests likely due to physical changes in the structure.

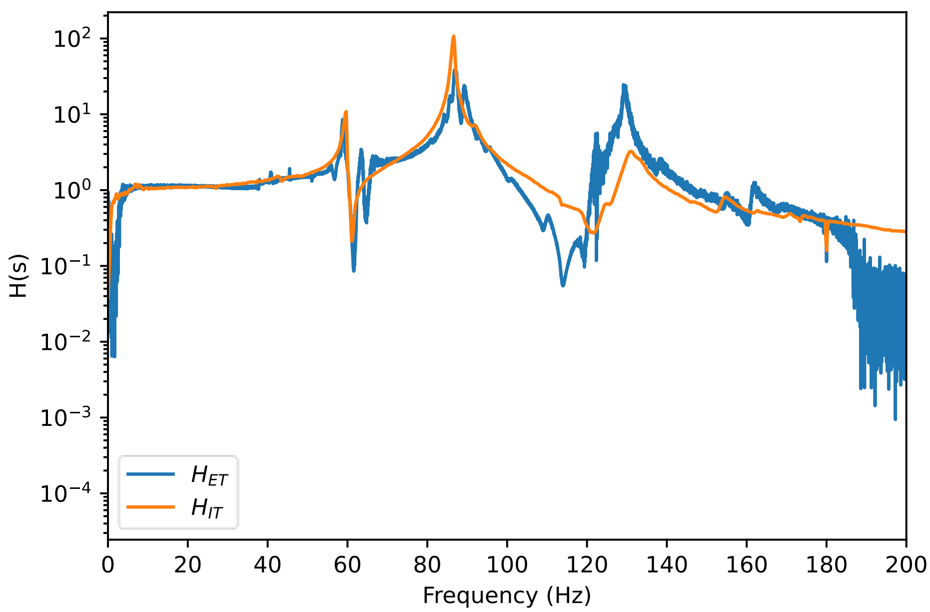

Figure 3.11. Comparison of the transfer functions of the electromagnet and impact tests.

Due to the dynamics of the system, H_{IT} contains both poles and zeros. The difference between these is that poles have an increased attenuation effect on the power at their frequencies while zeros have a decreasing attenuation effect. An important note about zeros is that they can alter signals to a point that they cannot be recovered. It was important that no important frequencies of the collected data fell on the sharp zero at around 60 Hz, so mass was added to the carriage to lower the operating frequency after inspecting the dynamics and comparing them to the dominant frequencies of the signal. The frequencies all fell on multiples of the operating frequency so 24 Hz was picked to avoid the zero of the system.

If the load cell was ideal and had no dynamics, H_{IT} would be equal to one for all frequencies. Looking at Figure 3.12, a dotted line is plotted to display the transfer function of an ideal sensor, H_{Ideal}. Comparing H_{IT} to H_{Ideal}, any frequencies of the signal where the content was above the ideal line was increased and below was decreased, meaning that the collected force data was distorted in these areas and had to be compensated for. The goal of compensation for this distortion was to scale the dynamics in a way that H_{IT} would settle at one for all frequencies to make it ideal. This was accomplished using inverse transfer function compensation.

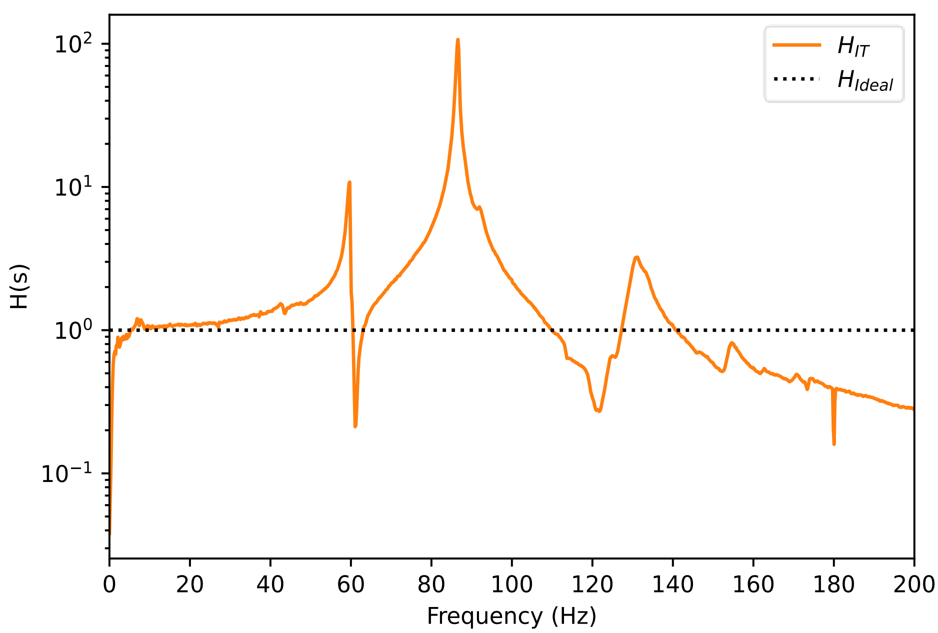

Figure 3.12. The load cell transfer function in comparison with an ideal transfer function to display the dynamic effects on the signal.

3.2.2 Inverse Transfer Function Compensation

Hobeck and Inman (2015) demonstrated the use of an inverse transfer function (ITF) compensation method to dynamically calibrate pressure probes with a trusted signal, negating the effects of acoustic attenuation on their output signal [27]. A similar method was implemented to filter the load cell data of this experiment. The ITF was used to design a digital filter to remove attenuation caused by load cell dynamics during postprocessing. Filtering H_{IT} with its inverse transfer function, H_{IT}^{-1}, is practically dividing $\mathrm{H_{IT}}$ by itself, counteracting the dynamic effects on the data. The frequency range chosen to fit the digital filter, F_{ITF}, to H_{IT}^{-1} was 10 to 200 Hz. All sensors have their own frequency bands in which they can extract their sensor specific measurement values from. The maximum frequency of 200 Hz was chosen because, upon inspection of the power spectrum of collected data from the load cell, the power content approached zero past 200 Hz. This indicates that it is incapable of accurately recording forces oscillating at frequencies above 200 Hz. The lower limit of 10 Hz was chosen because frequencies below this were not important to the signal produced by the experiment. The Python scipy.signal library functions zpk2tf, bilinear, and freqz were used to create and plot the frequency response of F_{ITF} as it was fit to H_{IT}^{-1}.

According to Smith (2007), pole-zero analysis can be used as a basis of digital filter design [28]. In pole-zero analysis, the transfer function of the filter takes on the form

$$H(z) = g\frac{(1-q_1z^{-1})+(1-q_2z^{-1})+\cdots+(1-q_Mz^{-1})}{(1-p_1z^{-1})+(1-p_2z^{-1})+\cdots+(1-p_Nz^{-1})} \tag{3.6}$$

in the z plane where q_i are the roots of the numerator, zeros, p_i are the roots of the denominator, poles, and g is the gain of the system. The recorded dynamics in H_{IT}^{-1} indicate the presence of underdamped poles and zeros in the bandwidth of the sensor. Inman (2014) demonstrated that the roots of underdamped systems take on the complex form

$$r_1, r_2 = -f_{zp} * \zeta_{zp} \pm f_{zp} * \sqrt{1 - \zeta_{zp}^2}\, i \tag{3.7}$$

where f_{zp} is the frequency of the pole or zero, ζ_{zp} is the specific damping ratio, and i is the imaginary unit [13]. The zpk2tf function took these individual roots and converted them to an analog filter in the s plane. From there, the bilinear function was used to build the digital filter in terms of the sampling frequency of the data it would filter, 2000 Hz. With this, the frequency response of F_{ITF} was plotted using freqz along with H_{IT}^{-1}. After the initial guess of F_{ITF} was set, the scipy.optimize.minimize function was used to enhance the accuracy of F_{ITF} compared to H_{IT}^{-1} using the sum squared difference of their log values as the value to be minimized. As shown in Figure 3.13, the final F_{ITF} used for filtering consisted of three poles and two zeros. The poles of a 4th order lowpass Butterworth filter and a pole at 1000 Hz were also implemented in F_{ITF} before the optimization to remove higher frequency content and ensure stability of the filter.

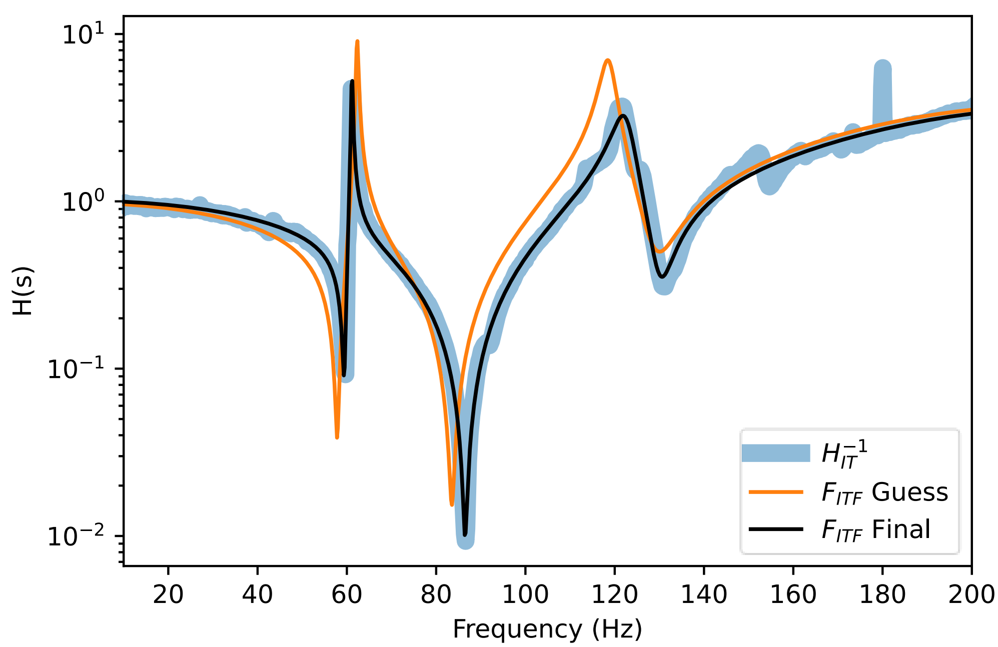

Figure 3.13. The ITF of the load cell displayed with the initial guess and the final optimized digital filter.

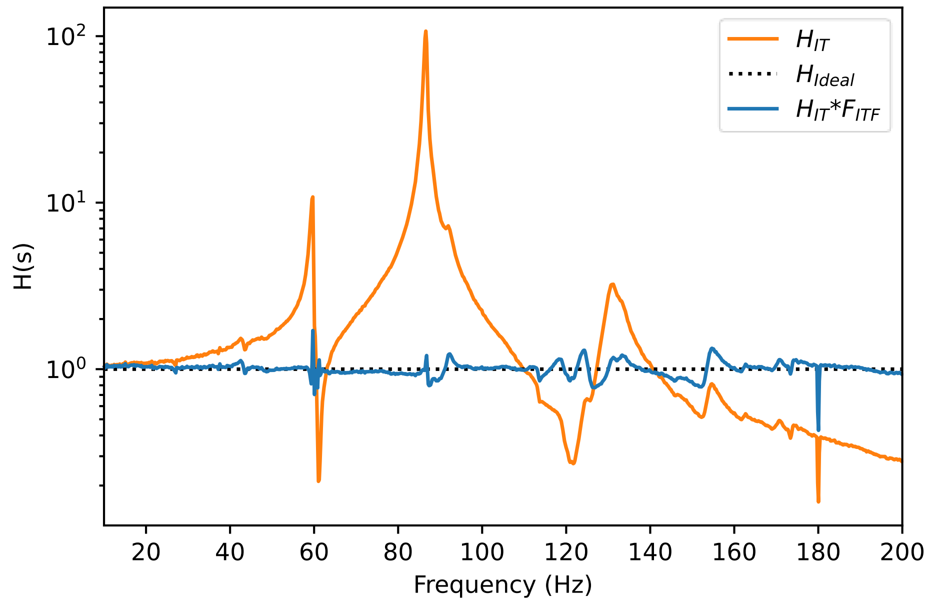

Figure 3.14. The effect of the digital filter on the transfer function of the load cell.

Figure 3.14 displays the effects the filter had on the system dynamics by multiplying H_{IT} by the frequency response of F_{ITF}. With the ability to compensate for load cell dynamics, final force data was extracted from the original signal. Since the force generated by the coil in this motion was periodic, the amplitudes had frequencies that dominated the time series wave making tall peaks compared to its noise floor. Unlike H_{IT}, when these peaks were plotted, they did not show a comprehensive picture of what the dynamics looked like but were still attenuated by the same dynamics of H_{IT}. Utilizing the lfilter function in Python, Figure 3.15 shows the filter effect on the time series signal while Figure 3.16 displays the effect the filter had on a force signal at an individual frequency. Table 3.1 displays the scaling effect on all five marked peaks in Figure 3.16. The square root of the PSD was taken because the power is directly proportional to the amplitude, or energy, squared. Each filtered peak was nearly equal to the unfiltered peak multiplied by the scaling value of F_{ITF} at that frequency, indicating that the filter functioned as intended. Using the ITF compensation method, the collected load cell data was filtered prior to making comparisons with simulated data.

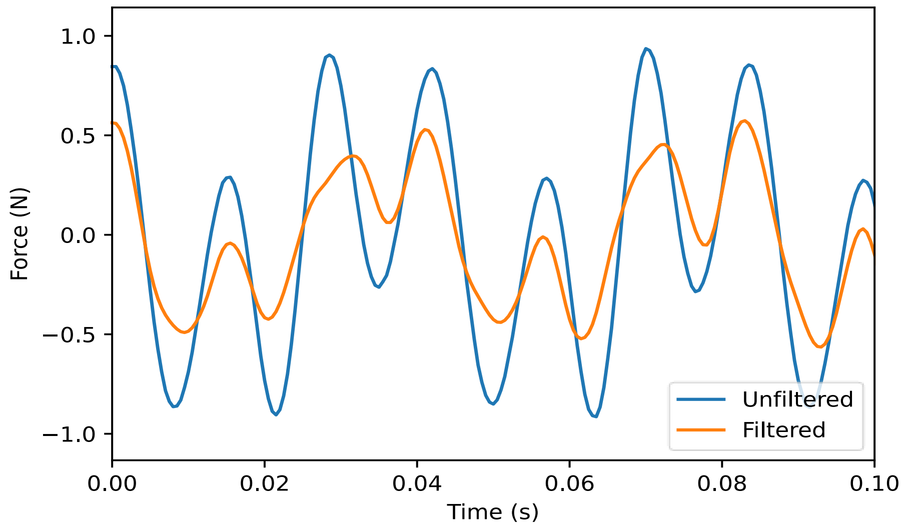

Figure 3.15. Filter effect on the time series digital signal from the 10 Ohm nominal resistive load, 0.69-cm peak-to-peak displacement experiment.

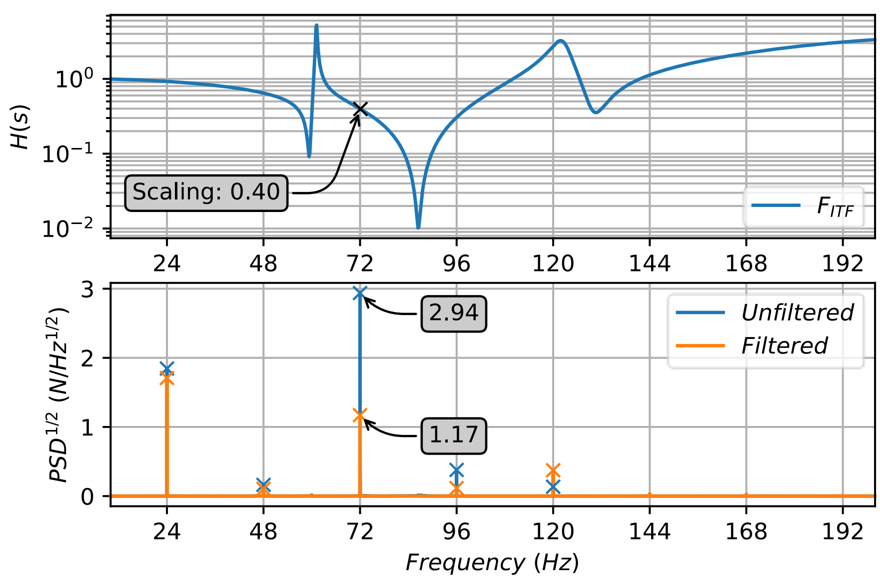

Figure 3.16. The scaling effect of the ITF filter on an amplitude peak of the force wave from the 10 Ohm nominal resistive load, 0.69-cm peak-to-peak displacement experiment.

Table 3.1. Scaling effect on the marked peaks in Figure 3.16

		Filter Values (N/Hz^0.5)	
Frequency (Hz)	Scaling	Unfiltered	Filtered
24	0.93	1.8450	1.7086
48	0.65	0.1625	0.1051
72	0.40	2.9371	1.1706
96	0.31	0.3783	0.1157
120	2.82	0.1357	0.3736

3.3 Finite Element Analysis of the Shaker Table Experiment

After data collection, the final experiments were modeled with the same recorded velocity, geometry, and material properties using FEA. The magnet was modelled as the mover and the coil was the stator in the simulation in order to reduce complexity of the model and simulation time. The modelled air of the simulation consisted of three parts: the outer air, inner air, and band. Figure 3.17 displays the cylindrical band that enclosed only the magnet with a diameter of 2.858-cm and length of 7.62-cm, allowing for the maximum magnet displacement from the experiments. The inner air was also a cylinder with a diameter of 4.445-cm and the same length as the band. The inner air enclosed the coil and was hollow for the band to fit inside it. The outer air consisted of a cube with sides of 25.4-cm each and the other parts centered inside it.

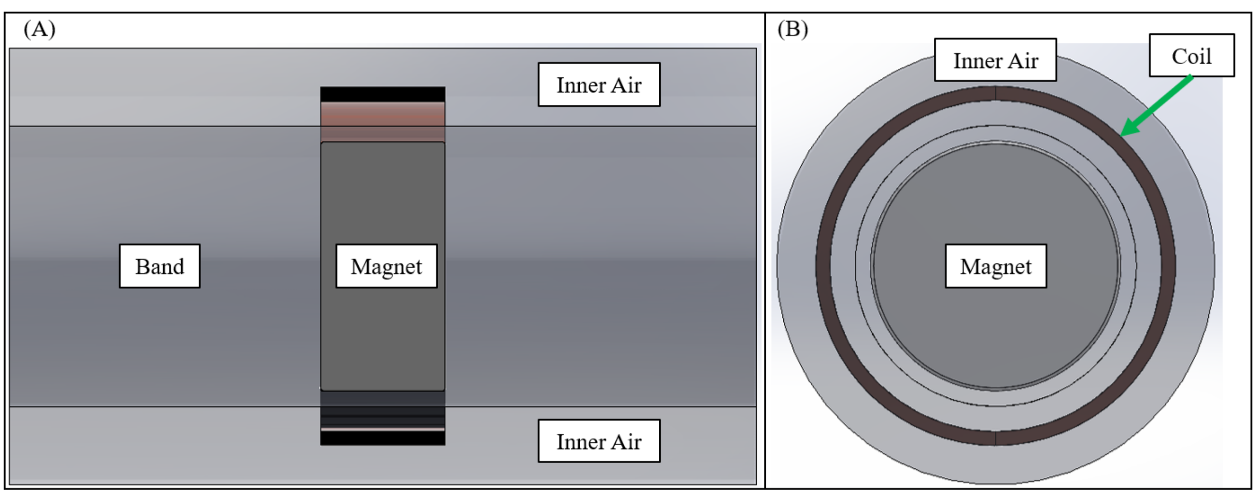

Figure 3.17. (A) Cross section front view of the refined smaller air components, magnet, and coil. (B) Side view of the same components.

After all the parts were modeled, the motion was assigned with the data points feature of the motion analysis tool. Using the experimental velocity data, the average peak-to-peak displacement of the motion was found. A csv file was made in excel with columns for the time elapsed and the position of the magnet, P_{mag}. The position of the magnet at each of these times was calculated with the sine function in the form

$$P_{mag} = A_p \sin\left(2\pi * f_m * t\right) \tag{3.8}$$

where A_p is the peak displacement, f_m is the motion frequency of 24 Hz, and t is the elapsed time. The data points were then uploaded to the motor motion analysis tool and the motion was assigned to the magnet in the direction keeping it concentric to the coil with its rotation locked.

For the resolution of the motion time steps, 2400 frames/s were chosen to make the data points evenly proportional with the 24 Hz motion. This was done to aid post processing of the FEA data by providing a straightforward way to pick out an end time in the time series signal to use for extracting one cycle in the data. Using this end time, the period of the motion, 1/24 Hz, was subtracted from it to give the time range of the cycle. The reason that the end time could not just be the period of the motion was because the simulation took a portion of time steps to reach its steady state operating values. The values of this range were copied and attached to the end of themselves as many times as needed without discontinuities in the sequence because the signal was periodic. This allowed for the time series data to be processed like the experimental data was and compared in the frequency domain with high resolution. The end time used for each simulation was 0.05 seconds which allowed for the completion of one full cycle and then some, making the start of the time range 0.0083 seconds.

After the motion was set, the transient magnetic study was defined. The N52 magnet remanence and coercive force were set to the documented BH curve values measured experimentally by KJ Magnetics. The value used for remanence was 14380 Gauss and coercivity was 11300 Oersted with its coercivity direction pointing along the direction of oscillation [22]. The measured coil resistance of the experiment was 10.7 Ohms. Using the geometry of the coil and the default conductivity of copper in the FEA software, 5.7e+07 S/m, the simulated coil resistance was estimated to be 9.93 Ohms. The missing 0.77 Ohm of resistance was placed in series with the resistive load and the coil to account for the missing resistance in the circuit case of the simulations. The wound coil was defined as in Chapter 2 but with 250 turns and a wire diameter of 0.2489 mm as the documentation described. The Lorentz force method is for calculating the electromagnetic force acting on a conductor material [18]. This method was used to calculate the force acting on the coil and was taken as equal and opposite of the force that opposed the magnet mover. [18]

The values needed for the FEA data comparison of the magnitudes were the voltage, or current, and force so the mesh independence study was run with those values in mind. The first step of the study was to determine the average mesh element size of each part in the system, provided in Table 3.2. Noting that the coil and magnet parts have similar element sizes while the band and inner air did as well, only two controls were used to converge the mesh by grouping these similar element sized parts together.

Table 3.2. Initial mesh element size of each part before mesh independence study of shaker table experiment.

Part Name	Average Mesh Element Size (mm)
1.27 cm 250 Turn Coil Half	1.71
1.27 cm 250 Turn Coil Half	1.71
1.27 cm Magnet	1.52
Band	3.45
Inner Air	3.95
Outer Air	35.20

After placing a 0.762-mm volume mesh control on the coil and magnet group and a 1.905 -mm volume control on the band and inner air components, it was determined mesh refinement had insignificant effects on the values. Since the simulation time was reasonable, these mesh controls were accepted for use in the simulations for comparison later. Table 3.3 displays the mesh effects on the mean squared error (MSE) of the accepted mesh between the default mesh, accepted mesh with the outer air element size halved, and the halving of the accepted mesh for the force and current signals for the minimum and maximum displacement of the 10 Ohm studies. The MSE was used because the most refined mesh took a large amount of time to simulate so only half of the full cycle of the signals were calculated. This same technique was applied for all the comparisons in Table 3.3 for consistency. The MSE was calculated with

$$SSE = \frac{1}{n}\sum_{i=0}^{n}[(Accepted\ Mesh)_i - (Different\ Mesh)_i]^2 \tag{3.9}$$

where i is the position of the data point in the signal for the respective mesh and n is the total number of data points. As seen, the MSE was very small for all the different meshes indicating the accepted mesh was sufficient for independent calculations.

Table 3.3. Mean square error of the accepted mesh from various meshes for the 10 Ohm minimum and maximum displacement studies. A hyphen under the mesh control sizes indicates that no change to the element size of that part was made and was the size shown in Table 3.2.

Mesh Indication	Volume Mesh Control Sizes (mm)			MSE Values			
				0.69 cm Displacement		4.24 cm Displacement	
	Magnet and Coil	Band and Inner Air	Outer Air	F_{RMS}, (N^2)	I_{RMS}, (A^2)	F_{RMS}, (N^2)	I_{RMS}, (A^2)
Accepted	0.762	1.905	-	-	-	-	-
Default	-	-	-	4.93E-07	2.41E-07	1.80E-04	1.12E-05
Outer Air Halved	0.762	1.905	17.60	2.79E-08	1.11E-08	9.46E-07	3.22E-08
Controls Halved	0.381	0.953	-	8.92E-08	2.89E-08	1.34E-05	1.44E-06

3.4 Experimental and Simulated Results of the Shaker Table Experiment

After looking at the time series data of the two values under inspection compared to the predicted FEA values plotted with the experimental and simulated velocity wave in Figure 3.18, it was rewarding to observe the shape of the waves resembled one another. Although these time series domain comparisons were pleasing to look at, they did not give measurable information regarding magnitude and frequency content that could be used to numerically compare them. Comparing the experimental and FEA simulated data had two major points of interest. The first was to compare the RMS values of the signals. The RMS of the signal supplies a way to compare two waveforms with an average that is specific to the waveforms themselves. By comparing the RMS of the signals, a good picture of similarities in the magnitudes of waveforms was found. The second point of interest was the energy distribution of the signals. Meaning the signal was qualitatively observed in the frequency domain to understand these waves and how they behaved according to the motion. This showed the dominant frequencies of the signal so the energy distribution of the time series data could be qualitatively compared. Using these two signal analysis methods, a strong comparison was made to support FEA as a prediction method for electrical power and electromagnetic force generated in linear alternators due to resistive loads.

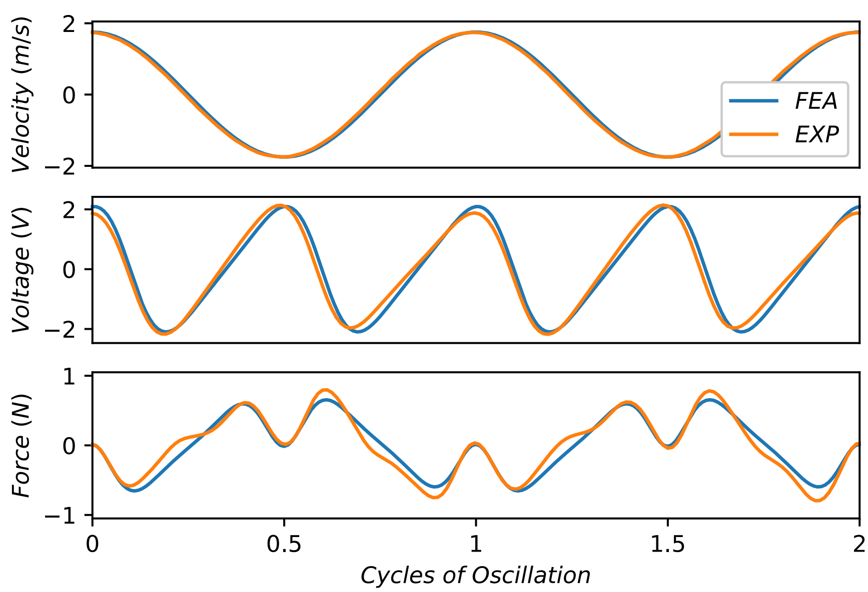

Figure 3.18. Time series data comparison of the 10 Ohm, 2.34-cm peak-to-peak displacement of the experimental and FEA simulated results plotted for two cycles of motion with each waveform individually shifted to start at the same peak in the pattern.

3.4.1 Post Processing of Collected Data

After data collection, all experimental force signals collected were processed using the same ITF compensation method described in section 3.2. A lowpass 4th order Butterworth filter at 200 Hz was also applied to the experimental coil voltage signal to remove high frequency content. For the simulated data, one cycle of the force and current signals for each study was copied and stitched together to form one long sequence of data. One 24 Hz cycle in the simulation set to 2400 frames/s, or samples/s, yielded an experimental samples per cycle of

$$f_{es} = \frac{2400\ samples/s}{24\ Hz} = 100\,\frac{samples}{cycle}. \tag{3.10}$$

The data was copied 1320 times to create a sequence of 132000 samples. The length of this sequence is equal to the minimum number of samples collected in the experiments. At 2400 samples/s the total equivalent time, t_{equiv}, of the sequence becomes

$$t_{equiv} = \frac{132000\ samples}{2400\ \frac{samples}{s}} = 55\ seconds. \tag{3.11}$$

The only conversions needed in post processing were the FEA coil current was used to find the voltage across the resistor using equation (2.4) and the vibrometer data had to be divided by 2 to convert it from 500 (mm/s)/V to 1 (m/s)/V.

3.4.2 RMS Comparisons

With the time series data processed, the RMS values of V_{RMS}, F_{RMS}, and the linear oscillation velocity of the mover, L_{RMS}, were used to compare the FEA and experimental signals. The reason velocity RMS was calculated and not displacement is because the common unit of damping force is depicted in force per velocity and is used in comparison later. Table 3.4 displays each peak-to-peak displacement along with its corresponding RMS velocities. With these values for the simulated and experimental signals, they were then compared to one another for validation of the FEA.

Table 3.4. Corresponding RMS velocity for the motion displacements of the experiments.

Peak-to-Peak Displacement (cm)	L_{RMS} (m/s)
0.69	0.37
1.52	0.81
2.34	1.24
3.30	1.76
4.24	2.25

The first comparison was made between the RMS voltages and power. Figure 3.19 (A) and (E) show the comparison of each FEA simulated RMS voltage and power generated for its RMS velocity plotted along the decade resistance sweep with the experimental counterparts. The values of each data point are also displayed in Figure 3.19 (B), (F), (C), & (G). The RMS power, P_{RMS}, was calculated using equation (2.6). Resistances above the nominal resistance of 1000 Ohms were left out because the voltage stopped increasing after this resistance as the load approached infinity. Originally, only the simulations for the resistance with the maximum P_{RMS} of their curves, 10 Ω, and the L_{RMS} that was in the middle of the collected velocities, 1.24 m/s, were to be run and compared to the experimental data. Examining Figure 3.19 (D) & (H), the percent differences of most of the values stay within a reasonable amount until reaching the lower L_{RMS} of 0.37 and 0.81 m/s. It is unknown why the percent difference was so large, but further inspection was done to see if the difference of these two velocities decreased as resistance approached infinity. The percent difference did decrease for these configurations, further supporting the use of FEA for these calculations. Overall, the FEA did well in predicting the voltage and power magnitudes of the system as the largest magnitudes of percent difference outside of the two lower velocities were 4.10% and 8.03%, respectively.

(A)

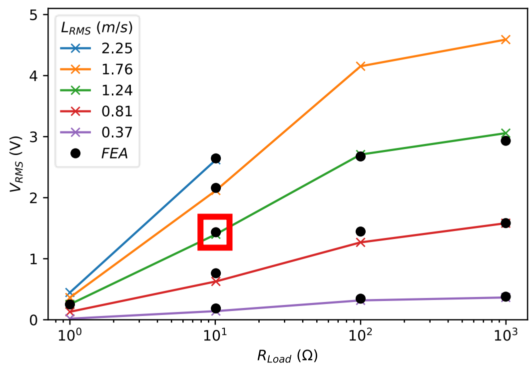

(E)

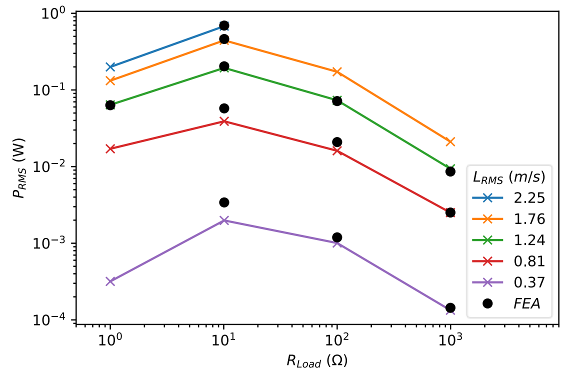

(B)

	Resistive Load, Nominal (Measured) Ω			
L_{RMS} (m/s)	1 (1)	10 (10.1)	100 (100)	1000 (997)
2.25	0.447	2.620	-	-
1.76	0.364	2.118	4.153	4.590
1.24	0.253	1.400	2.707	3.057
0.81	0.131	0.628	1.267	1.582
0.37	0.018	0.142	0.317	0.365

(F)

	Resistive Load, Nominal (Measured) Ω			
L_{RMS} (m/s)	1 (1)	10 (10.1)	100 (100)	1000 (997)
2.25	0.19972	0.67967	-	-
1.76	0.13217	0.44406	0.17248	0.02113
1.24	0.06393	0.19402	0.07327	0.00937
0.81	0.01705	0.03904	0.01606	0.00251
0.37	0.00032	0.00198	0.00101	0.00013

(C)

	Resistive Load, Nominal (Measured) Ω			
L_{RMS} (m/s)	1 (1)	10 (10.1)	100 (100)	1000 (997)
2.25	-	2.644	-	-
1.76	-	2.160	-	-
1.24	0.251	1.434	2.675	2.932
0.81	-	0.762	1.445	1.583
0.37	-	0.186	0.346	0.379

(G)

	Resistive Load, Nominal (Measured) Ω			
L_{RMS} (m/s)	1 (1)	10 (10.1)	100 (100)	1000 (997)
2.25	-	0.69194	-	-
1.76	-	0.46203	-	-
1.24	0.06322	0.20357	0.071568	0.0086203
0.81	-	0.05751	0.020884	0.0025149
0.37	-	0.00341	0.001194	0.000144

(D)

	Resistive Load, Nominal (Measured) Ω			
L_{RMS} (m/s)	1 (1)	10 (10.1)	100 (100)	1000 (997)
2.25	-	0.90	-	-
1.76	-	2.00	-	-
1.24	-0.56	2.43	-1.17	-4.10
0.81	-	21.36	14.02	0.12
0.37	-	31.13	8.99	3.77

(H)

	Resistive Load, Nominal (Measured) Ω			
L_{RMS} (m/s)	1 (1)	10 (10.1)	100 (100)	1000 (997)
2.25	-	1.81	-	-
1.76	-	4.05	-	-
1.24	-1.12	4.92	-2.32	-8.03
0.81	-	47.29	30.00	0.23
0.37	-	71.94	18.79	7.69

Figure 3.19. (A) & (E) The plots of the FEA simulated and experimental RMS voltage and power, respectively. (B) & (F) The values in the black outline box are the experimental RMS voltages and powers, respectively, in position in the table according to their positions in plots (A) & (E), this organization applies to the other tables as well. (C) & (G) are the FEA RMS voltages and powers, respectively. (D) & (H) are the percent differences of the available FEA values from the experimental RMS voltages ((C) from (B)) and powers ((G) from (F)), respectively. NOTE: The red box appearing in (A)-(D) serves as a guide for the organization of these figures by identifying a set of points that correspond to one another like the others in the figures.

From there, the RMS force values were compared. After the experimental results were processed, F_{RMS} of each resistive load was plotted along L_{RMS} to observe the effect the velocity had on the force. Observing Figure 3.20, a pattern was quickly noticed in the three lower resistance curves that resembled an inflection point near 1.24 m/s. All resistance curve forces were divided by the F_{RMS} value at 1.76 m/s which normalized the values. Then, these values were plotted in Figure 3.21 to further expose the pattern between the curves.

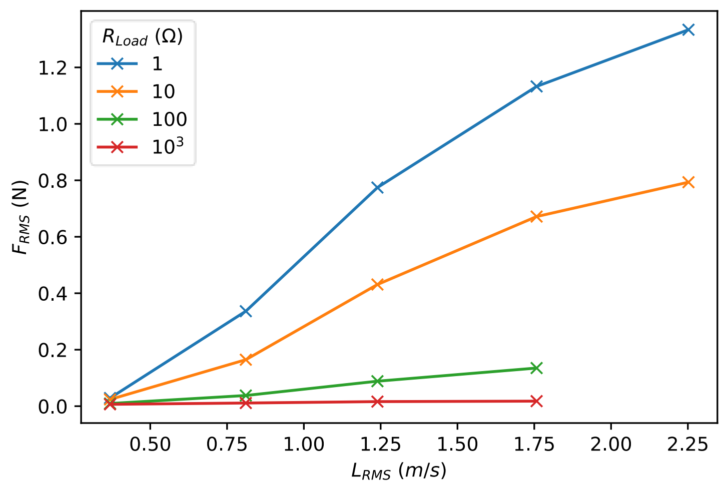

Figure 3.20. Experimental RMS force data of each decade of the resistance sweep plotted along the RMS velocity.

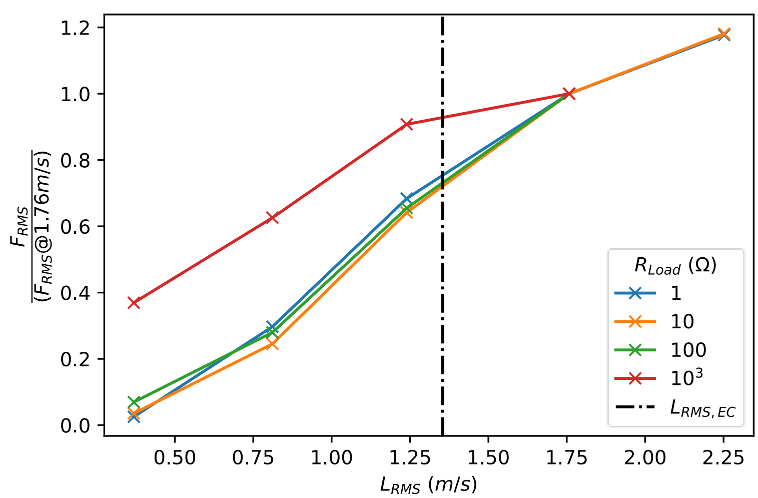

Figure 3.21. The normalized force of the resistance curves displaying the nonlinear pattern in the data along with the velocity at which the magnet exited the coil.

Besides the 1000 Ω curve outlier that will be discussed later, all three of the lower resistance curves showed the same nonlinear behavior. This was an important observation as this depicts the damping force as being a nonlinear function of velocity as was expected to find. The derivative of equation (3.8) reveals the velocity equation of the motion written in the form

$$V_p = 2\pi * 24 * A_p * \cos(2\pi * 24 * t). \tag{3.12}$$

The maximum amplitude, i.e., when the cosine function is one, was all that was needed to find the RMS velocity at which the magnet fully left the coil during oscillation. The maximum amplitude needed to leave the coil was 2.54-cm, or 0.0254 meters. This value yields the peak velocity of 1.92 m/s. Since it was cosine motion, the RMS velocity at which the magnet exited the coil, $L_{RMS,EC}$, was determined using

$$L_{RMS,EC} = \frac{V_p}{\sqrt{2}} \tag{3.13}$$

which yielded 1.35 m/s. Plotting this value vertically in Figure 3.21 shows that its position in the resistance curves is coincident with the inflection point, suggesting the damping force was affected by the coil-to-magnet length ratio and the peak-to-peak displacement of the motion. After this, these experimental results were compared with the FEA results.

Figure 3.22 (A) shows the same plot as Figure 3.20 with the simulated results and the line indicating when the magnet began leaving the coil. Immediately standing out in Figure 3.22 (D) are the large magnitudes of percent differences (the ones greater than 47%) between the 1000 Ω results and for one of the 100 Ω results. As resistive load increases, the current will decrease resulting in a weaker electromagnetic force as shown in Figure 3.22 (A). At these small currents, the force may have been so small that it was covered up by the noise in the system. For the three RMS velocities of the values in question, 0.37, 0.81, and 1.25 m/s, the RMS of the noise floor,

(A)

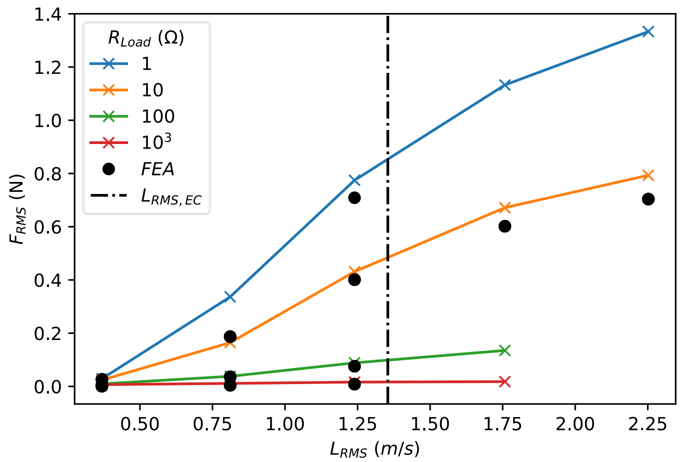

(B)

Resistive Load, Nominal (Measured) Ω	L_{RMS} (m/s)				
	0.37	0.81	1.24	1.76	2.25
1 (1)	0.0286	0.3363	0.7746	1.1327	1.3339
10 (10.1)	0.0238	0.1646	0.4310	0.6716	0.7933
100 (100)	0.0094	0.0378	0.0884	0.1350	-
1000 (997)	0.0066	0.0111	0.0162	0.0178	-

(C)

Resistive Load, Nominal (Measured) Ω	L_{RMS} (m/s)				
	0.37	0.81	1.24	1.76	2.25
1 (1)	-	-	0.7089	-	-
10 (10.1)	0.0261	0.1869	0.4010	0.6017	0.7037
100 (100)	0.0049	0.0361	0.0757	-	-
1000 (997)	0.0005	0.0040	0.0083	-	-

(D)

Resistive Load, Nominal (Measured) Ω	L_{RMS} (m/s)				
	0.37	0.81	1.24	1.76	2.25
1 (1)	-	-	-8.49	-	-
10 (10.1)	9.94	13.58	-6.95	-10.41	-11.29
100 (100)	-47.68	-4.52	-14.40	-	-
1000 (997)	-91.80	-64.45	-48.53	-	-

Figure 3.22. (A) Plot of the FEA and experimental RMS force results along with line indicating when the magnet exited the coil. (B) The values in the black outline box are the experimental RMS forces in position in the table according to their positions in plot (A), this organization applies to tables (C) & (D) as well. (C) The FEA values of the RMS forces. (D) The percent differences of the available FEA values (C) from the experimental RMS forces (B).

calculated with equation (2.2), were 0.00679, 0.00679, and 0.00832 N, respectively. After looking at the predicted values for these configurations in Figure 3.22 (C), they suggested that the magnitude of the electromagnetic force was less than or nearly equal to the magnitude of the noise. This gave reason to conclude that the force was not accurately recorded for those sets of data.

Looking at the FEA results of the 10 Ω values shows that a similar inflection was calculated in the software like what was seen in the experimental data. This showed that FEA can handle the different geometries and motion of the linear alternator to make accurate electromagnetic force predictions where most of the values fell within 15% of their experimental counterparts. In terms of the RMS comparisons, the FEA highlighted its ability to accurately predict the magnitudes of the periodic power and force dependent upon the resistive loads and mover velocity generated by most configurations of the experimental system.

3.4.3 Power Spectrum Comparisons

Moving on from the RMS results, it was expected that due to the observed inflection point of the force data as velocity was increased, there would also be a noticeable shift in the frequency domain as velocity was increased. Figure 3.23 utilizes the normalized energy distribution of all experiments run and simulated with the 10 Ω resistor to compare the effects of L_{RMS} on the frequency content of the signals. The distributions were normalized by dividing the entire domain by its largest peak, making the frequency with the maximum amplitude equal to one and the rest a proportion to it. The energy distributions for the experimental and FEA signals were then plotted over one another with x's of their respective colors marking their peaks.

Figure 3.23 shows that for all the studies, the 24 Hz original frequency was the most dominant of all the frequencies for both the simulated and experimental force signals. Past this frequency, as L_{RMS} increased a shift in energy from the 72 to 120 to 168 Hz frequencies occurred meaning the frequencies with the most energy in relation to the maximum amplitude changed. Coincidently, all these frequencies are the odd multiples of 24 Hz. Remembering the magnet began exiting the coil between the 1.24 and 1.76 m/s RMS velocities, an interesting observation was made that the 72 and 120 Hz frequencies trade which one has the most energy proportional the maximum amplitude between those velocities, or displacements.

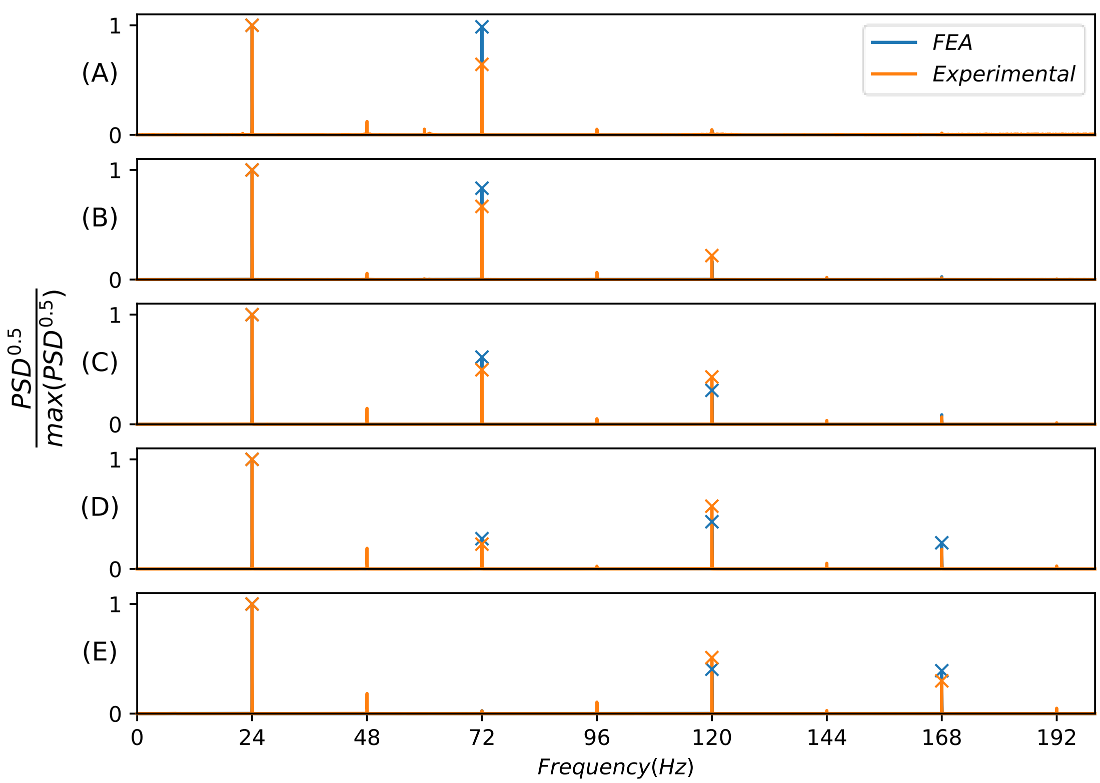

Figure 3.23. Normalized energy distribution for each force signal collected and simulated with the 10 Ohm resistive load. RMS velocity of each plot: (A) 0.37 m/s (B) 0.81 m/s (C) 1.24 m/s (D) 1.76 m/s (E) 2.25 m/s.

The same comparison was then made with the voltage data in Figure 3.24. The signal for the voltage starts as just a 48 Hz wave. As the velocity increased the even multiples of 48 Hz began to gain energy. Overall, the experimental voltage comparison matched the simulated data, while the force had small discrepancies, but behaved as expected in comparison with one another with the increasing L_{RMS}. This frequency domain comparison shows that the software correctly modeled the frequency content of the time series force and voltage data according to mover velocity.

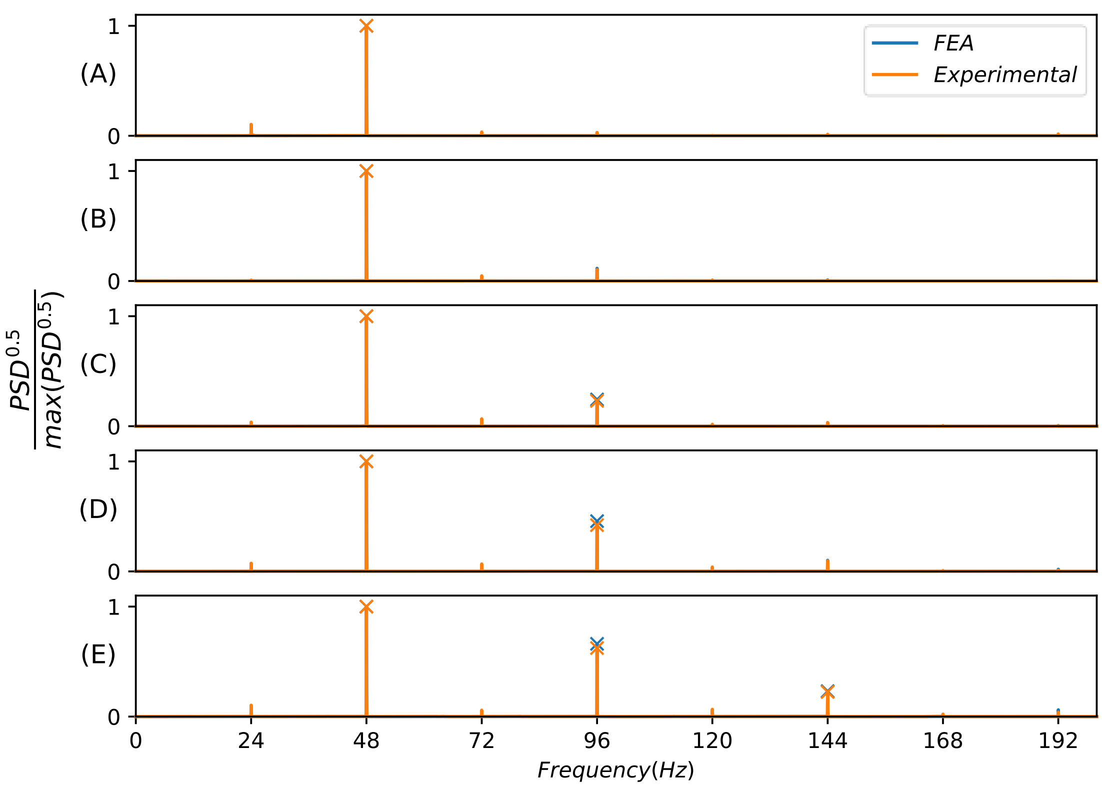

Figure 3.24. Normalized energy distribution for each voltage signal collected and simulated with the 10 Ohm resistive load. RMS velocity of each plot: (A) 0.37 m/s (B) 0.81 m/s (C) 1.24 m/s (D) 1.76 m/s (E) 2.25 m/s.

3.5 Summary and Conclusions

This chapter details how FEA was validated to model the electromagnetic force and electrical power generated due to resistive loads by linear alternators through comparison of experimental and simulated results. The final experiment utilized a shaker table to linearly oscillate a coil (mover) around a magnet (stator). With this prescribed motion, values similar to what would be generated by a linear alternator were observed. A limitation of the peak-to-peak displacement of the shaker table created a problem as the larger magnets available for use were too long to be implemented in the experiment. In order to solve this problem, a fixture was designed and built for the shaker table using the base excitation of a 1 DOF mass-spring system model to increase the maximum peak-to-peak displacement beyond that of the shaker table by itself. Employment of this mass-spring system also allowed for the operation frequency to be tuned as needed for the experiment.

The magnet was coupled to a load cell for force measurement using the attraction force between the magnet and a steel screw fastened to the load cell. There were concerns about vibration propagating through the structure holding the load cell, so a weighted down table was employed to support an adjustable holding arm with the load cell fastened to it. The arm was then used to align the magnet within the coil using two 3D printed sleeves to guide it into place.

With the physical experiment setup, the time series data sets needed to model and compare it with simulation were mover velocity, coil voltage across different resistive loads, and electromagnetic force. Since the load cell measurement requires a bridge module, a cDAQ was used to collect all three measurements simultaneously. Five peak-to-peak displacements of oscillation were used as data collection points ranging most of the available maximum displacement allowed by the fixture. For each collection point, except for the largest displacement, a resistive load decade sweep was performed. Calculations for the frequency resolution of fast Fourier transforms were performed prior to data collection to ensure enough time series data was saved for frequency domain comparisons later.

It was noticed that the load cell used for electromagnetic force collection displayed dynamics which distorted the force signal output from the sensor. An impact hammer test was implemented to characterize the transfer function of the load cell while it was still in position for the experiment. The ITF was then used to design and optimize a digital filter in Python that could counteract the effects of the load cell dynamics on the force signal in postprocessing. After the digital filter was built and tested, it was employed to filter the force data for comparisons with the simulated results.

The results of these experimental methods were then used to build a finite element model of the experiment to provide simulated data for comparisons of the two methods. The coil and magnet were both modeled with the same techniques as described in Chapter 2, with differences in the modeling values that remained in accordance with the documentation and physical properties of them. The force acting on the coil in this simulation was taken to be equal and opposite of the force opposing the magnet motion. Using the Lorentz force method to calculate this force on the coil, it was used for comparison with the experimentally collected force on the magnet. The sample rate of the software calculations was defined in a way that one data cycle could be copied and pasted to the end of itself. This was done in postprocessing until a sequence long enough to have a high-resolution frequency domain comparison with the experimental results was generated. With these simulated and experimental results, comparisons between the RMS and frequency content of the signals were made.

The RMS comparison of the coil voltage over a resistive load, electrical power, and electromagnetic force signals showed that the simulation yielded similar results in terms of magnitude to the experiment. Each comparison demonstrated the same behaviors when plotted side by side. The RMS voltage and power comparison displayed that most values for the finite element model fell within 4.10% and 8.03% difference from their experimental counterparts, respectively. The RMS force comparison also displayed that almost all the simulated values that were not similar in magnitude to the noise floor of the experimental system fell within 15% difference from the experiments. This RMS comparison presented that, even with the linear simplification of the BH curve of the magnet, the finite element model can calculate the necessary field values to find the magnitudes of the electromagnetic force and electrical power generated. Looking closer at the force plots in Figure 3.22 (A), the software also demonstrated the ability to correctly calculate the nonlinear damping force of an alternator as it changes with RMS velocity, thus satisfying the requirements for the project.

The frequency domain comparisons show that each simulated signal can accurately predict the energy distribution of the force and voltage signals according to the relation of the magnet motion to the coil and the magnet-to-coil length ratio. This was exhibited by how it correctly predicted the energy shift as RMS velocity increased in Figure 3.23 and Figure 3.24. By displaying this agreement along with the RMS comparisons for an experiment that resembled a linear alternator, FEA supplied a method to achieve the two main objectives for this research:

1. Experimentally validate a finite element model of a linear alternator.
2. Characterize the relationships between the electromagnetic force, mover velocity, resistive load, and power output of a linear alternator.

Using the finite element modelling approach detailed in this chapter, linear alternator properties that affect the efficiency of a MICE can be simulated and integrated with the combustion and kinematics models designed by the research team. With this, FEA was validated and proposed for further use in the research project and other research applications pertaining to linear alternators.

Chapter 4

Conclusions and Recommendations

4.1 Master Summary

This thesis presents an experimentally validated finite element modeling approach for predicting properties of linear alternators that affect the performance of FPEs they are coupled to. The basic requirements of the experiment needed to validate the finite element model were to generate a measurable coil voltage across a resistive load and electromagnetic force acting against a known relative motion of a permanent magnet passing through a coil. Using this known motion, the experiment could then be virtually modeled and compared with the simulated results to show the capability of the software to accurately predict these values of interest. The following serves as a summary of Chapter 2 and Chapter 3 which detail the methods used for this validation.

The initial experiment in Chapter 2 was used to explain how the simulation software worked while also providing a voltage and power comparison and insight on how the electromagnetic force needed to be measured. The experiment consisted of a test where a magnet was dropped through a coil to measure its motion and voltage across different resistive loads. The motion was collected using a vibrometer in hopes to extract a change in the velocity of the magnet for an electromagnetic force calculation. It was discovered later that because vibrometers are designed to collect linear oscillatory motion, the motion of the magnet moving in only one direction could not be accurately measured. Although the force calculation was not made, the vibrometer data was still used to estimate the velocity of the magnet moving through the center of the coil.

With this velocity data, FEA was used to simulate the experimental system by modeling the air and electronics parts, motion, magnet, coil, and circuit. The comparison of the voltage and power generated in the coil showed agreement between simulated and experimental results. After seeing the deficiencies from this experiment that resulted in the failure to accurately measure the force acting against the magnet, a final experiment was designed that compensated for these weaknesses and directly measured the electromagnetic force.

The final experiment discussed in Chapter 3 utilized a mass-spring fixture excited by a shaker table to oscillate a coil around a magnet coupled to a load cell for force measurement. The fixture provided a way to increase the maximum peak-to-peak displacement beyond the capability of the shaker table. This motion generated results for coil voltage and electromagnetic force that were similar to the values that are produced in linear alternators. By modeling the motion of this system with finite element analysis, the simulated and experimental results for the collected values could be compared. Due to the discovery of dynamics in the load cell used to collect the electromagnetic force data, a compensation method had to be implemented to remove signal attenuation. Through ITF compensation, the dynamic effect on the force signals was digitally filtered in postprocessing so the force signal could be accurately compared with simulated data.

Using the FEA software to calculate the voltage and force output of the experiment, comparisons between the RMS and frequency domain of the signals were made. These signal analysis tools provided a way to truly see how the signals of the two methods compared in both magnitude and energy distribution. The results showed good agreement between simulated and experimental RMS electrical comparisons along changing resistive loads. The RMS force comparison presented a damping force that displayed a nonlinear behavior as velocity was increased as was expected. This, along with comparison of the energy distribution shifts as mover displacement increased showed finite element modeling was capable of accounting for the magnet and coil dimensions and mover velocity. The finite element model thus displayed the ability to correctly predict the relationships between the nonlinear electromagnetic damping force, mover velocity, resistive load, and power output of the experiment mimicking a linear alternator. With this, the research team was provided the tools needed to numerically integrate a linear alternator model with the existing combustion and kinematics model of a FPE.

4.2 Recommendations for Future Work

With the criteria met for this part of the associated project, work still needs to be done to complete it. Looking past the research project the study originated from, there are other applications these findings can be applied to. The following is a bulleted list of recommendations for future work inspired by this research:

- The model validated in this research only displayed calculated values for an experimental system. The research team must use FEA to integrate the engine models with an alternator model. This requires the simulation of engine specific characteristics to generate the values expected for the system. With these characteristics, numerical methods can be used to construct the comprehensive engine model.
- This model has proven its ability to account for the simple geometries of a magnet and coil along with the relative motion of the system, now it can be used to model complex geometries. With this ability, an optimization study that identifies the optimal characteristics of these linear alternators would be valuable.

- The use of linear alternators can be applied to more than just UAVs. The compact nature of HEDCS creates many avenues for power generation applications in remote or cramped areas. Feasibility studies on the domains where these systems can be used for space efficient energy supply need to be conducted. With this knowledge along with methods to model these systems, research and industry can utilize this information to normalize their application in everyday power generation.

References

1. Depcik, C., Cassady, T., Collicott, B., Burugupally, S. P., Li, X., Alam, S. S., … Hobeck, J. (2020). Comparison of lithium ion Batteries, hydrogen fueled combustion Engines, and a hydrogen fuel cell in powering a small Unmanned Aerial Vehicle. *Energy Conversion and Management*, *207*. https://doi.org/10.1016/j.enconman.2020.112514
2. Surampudi, R., Blosiu, J., Bugga, R., Brandon, E., Smart, M., Elliott, J., … Cutts, J. A. (2017). *Energy Storage Technologies for Future Planetary Science Missions Work Performed under the Planetary Science Program Support Task*. Retrieved from https://solarsystem.nasa.gov
3. NASA Armstrong Flight Research Center. (2020, September 21). Unmanned Aerial Vehicles. Retrieved March 22, 2023, from https://www.nasa.gov/centers/armstrong/images/UAV/index.html
4. Alam, S. S., Rosa, S. W., Depcik, C., Preetham Burugupally, S., McDaniel, E., & Hobeck, J. D. (2021). Modification of the Wiebe function for methane-air and oxy-methane- based spark-ignition engines. *Fuel*, *303*. https://doi.org/10.1016/j.fuel.2021.121218
5. Vezirocjlu, T. N., & Barbir, F. (1992). *HYDROGEN: THE WONDER FUEL*. *Int. J. Hydrogen Energy* (Vol. 17).
6. Lonnie Shekhtman. (2019, November 12). With Mars Methane Mystery Unsolved, Curiosity Serves Scientists a New One: Oxygen.
7. Breeze, P. (2018). Stirling Engines and Free Piston Engines. In *Piston Engine-Based Power Plants* (pp. 59–70). Elsevier. https://doi.org/10.1016/b978-0-12-812904-3.00006-9
8. Yingcong, Z., Sofianopoulos, A., Lawler, B., & Mamalis, S. (2018). Advanced combustion free-piston engines: A comprehensive review. *Sage Journals*, *21*(7).
9. Hanipah, M. R., Mikalsen, R., & Roskilly, A. P. (2015, January 22). Recent commercial free-piston engine developments for automotive applications. *Applied Thermal Engineering*. Elsevier Ltd. https://doi.org/10.1016/j.applthermaleng.2014.09.039
10. Hosch, W. (Ed.). (n.d.). alternator. In *Encyclopedia Brittanica*. Retrieved from https://www.britannica.com/technology/alternator
11. Gergersen, E. (Ed.). (n.d.). Faraday's law of induction. In *Encyclopedia Britannica*. Retrieved from https://www.britannica.com/science/Faradays-law-of-induction

12. Gregersen, E. (Ed.). (n.d.). Lenz's law. In *Encyclopedia Brittanica*. Retrieved from https://www.britannica.com/science/Lenzs-law
13. Inman, D. J. (2014). *Engineering vibration* (4th ed.). Pearson.
14. Jia, B., Zuo, Z., Tian, G., Feng, H., & Roskilly, A. P. (2015). Development and validation of a free-piston engine generator numerical model. *Energy Conversion and Management*, *91*, 333–341. https://doi.org/10.1016/j.enconman.2014.11.054
15. Metscher, J. F., & Lewandowski, E. J. (2015). *Development and Validation of Linear Alternator Models for the Advanced Stirling Convertor*.
16. Khatri, P., & Wang, X. (2020, April 27). Comprehensive review of a linear electrical generator for ocean wave energy conversion. *IET Renewable Power Generation*. Institution of Engineering and Technology. https://doi.org/10.1049/iet-rpg.2019.0624
17. Comsol. (2016, March 15). The Finite Element Method (FEM). Retrieved March 22, 2023, from https://www.comsol.com/multiphysics/finite-element-method
18. EMWorks. (n.d.). *EMS Online Users Guide*. Retrieved from https://www.emworks.com/
19. Gregersen, E. (Ed.). (n.d.). displacement current. In *Encyclopedia Brittanica*. Retrieved from https://www.britannica.com/science/displacement-current
20. KJ Magnetics. (n.d.). Neodymium Magnet Information. Retrieved March 22, 2023, from https://www.kjmagnetics.com/neomaginfo.asp
21. National Instruments. (n.d.). NI CompactDAQ Chassis. Retrieved March 22, 2023, from https://www.ni.com/en-us/shop/hardware/products/compactdaq-chassis.html
22. KJ Magnetics. (n.d.). Demagnetization (BH) Curves for Neodymium Magnets. Retrieved March 22, 2023, from https://www.kjmagnetics.com/bhcurves.asp
23. KJ Magnetics. (n.d.). Neodymium Magnet Physical Properties. Retrieved March 22, 2023, from https://www.kjmagnetics.com/specs.asp
24. School of Engineering Brown University. (n.d.). Introduction to Dynamics and Vibrations. Retrieved March 23, 2023, from https://www.brown.edu/Departments/Engineering/Courses/En4/Notes/vibrations_forced/vibrations_forced.htm
25. Tan, L. (2008). *Digital Signal Processing*. Elsevier.
26. Ewins, D. J. (1994). *Modal Testing: Theory and Practice*. Research Studies Press LTD.

27. Hobeck, J. D., & Inman, D. J. (2015). Low-Cost Pressure Probe Sensor for Predicting Turbulence-Induced Vibration From Invasive Low-Velocity Turbulent Flow Measurements. *IEEE Sensors Journal*, *15*(8), 4373–4379. https://doi.org/10.1109/JSEN.2015.2419454

28. Smith III, J. (2023, January 9). Pole-Zero Analysis. Retrieved March 22, 2023, from https://ccrma.stanford.edu/~jos/fp/Pole_Zero_Analysis_I.html

Appendix A - Coil Dimensions for Drop Test Experiment

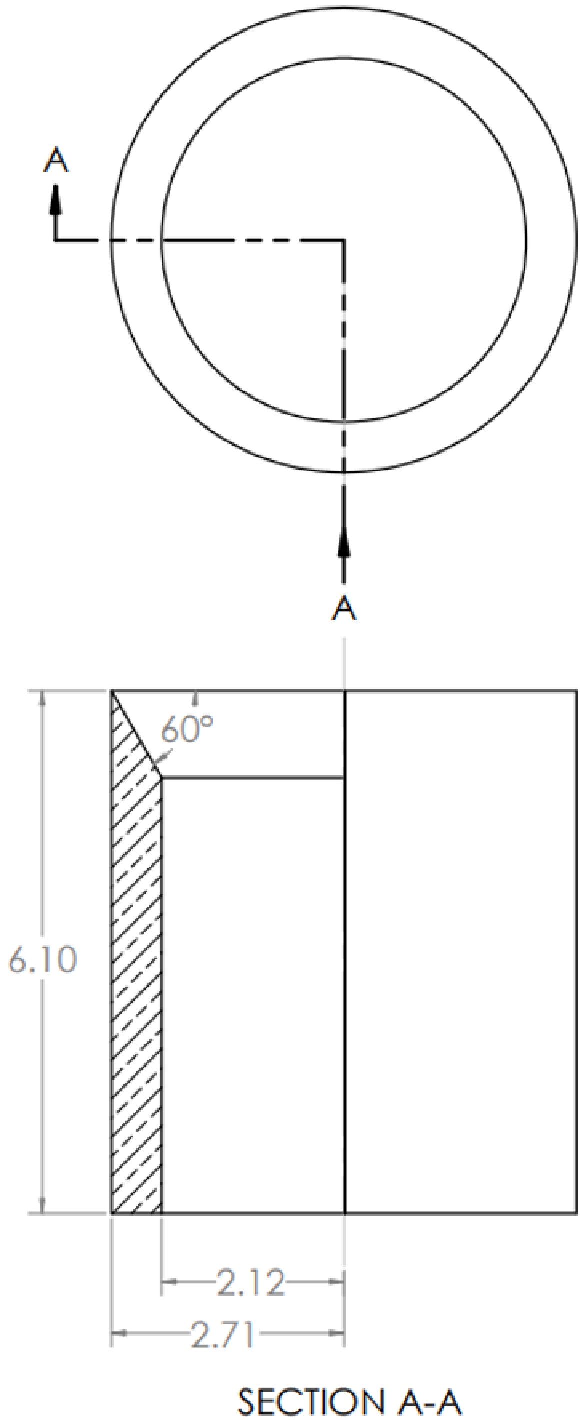

Figure A.1. Dimensioned drawing of the coil used for the drop test experiment with lengths in units of centimeters.

Appendix B - Drop Test Experiment LabView VI

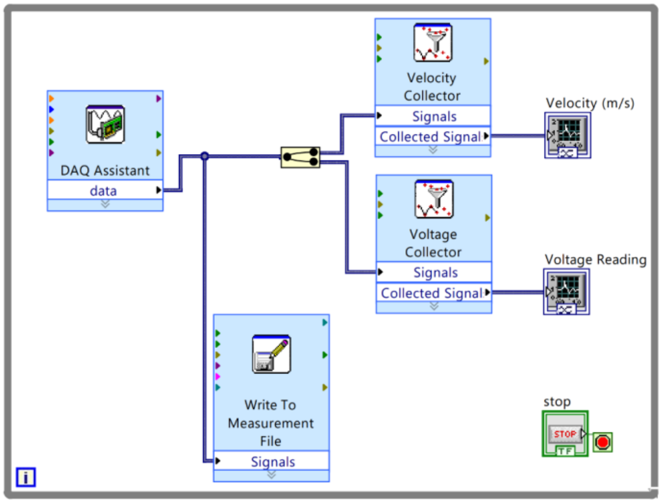

Figure B.1. Block diagram of the drop test VI used to collect coil voltage across a resistive load and magnet velocity.

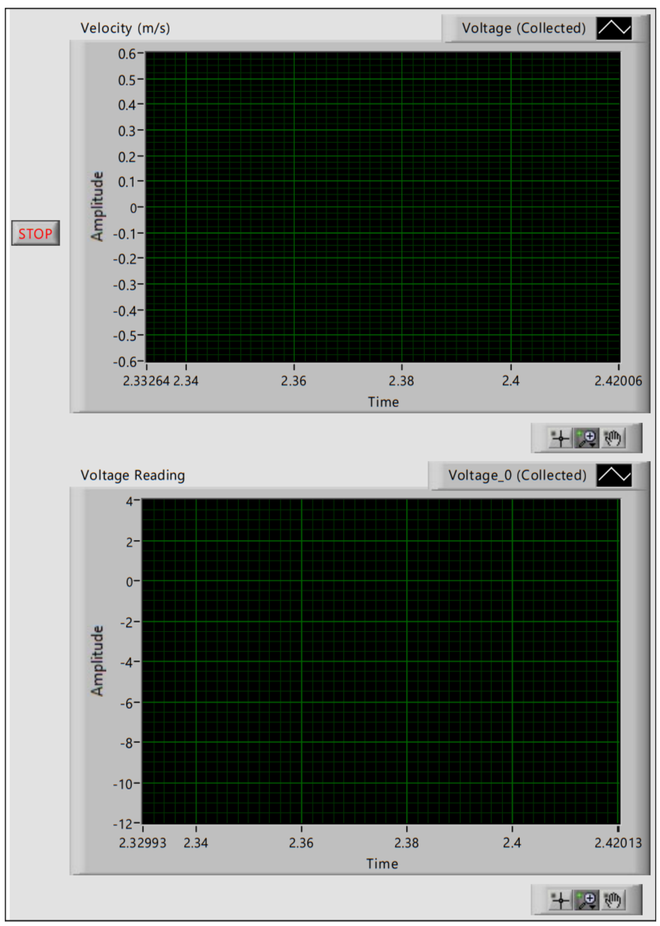

Figure B.2. Front panel of the drop test VI used to display the real time voltage across a resistive load and magnet velocity.

Appendix C - Shaker Table Experiment LabView VI

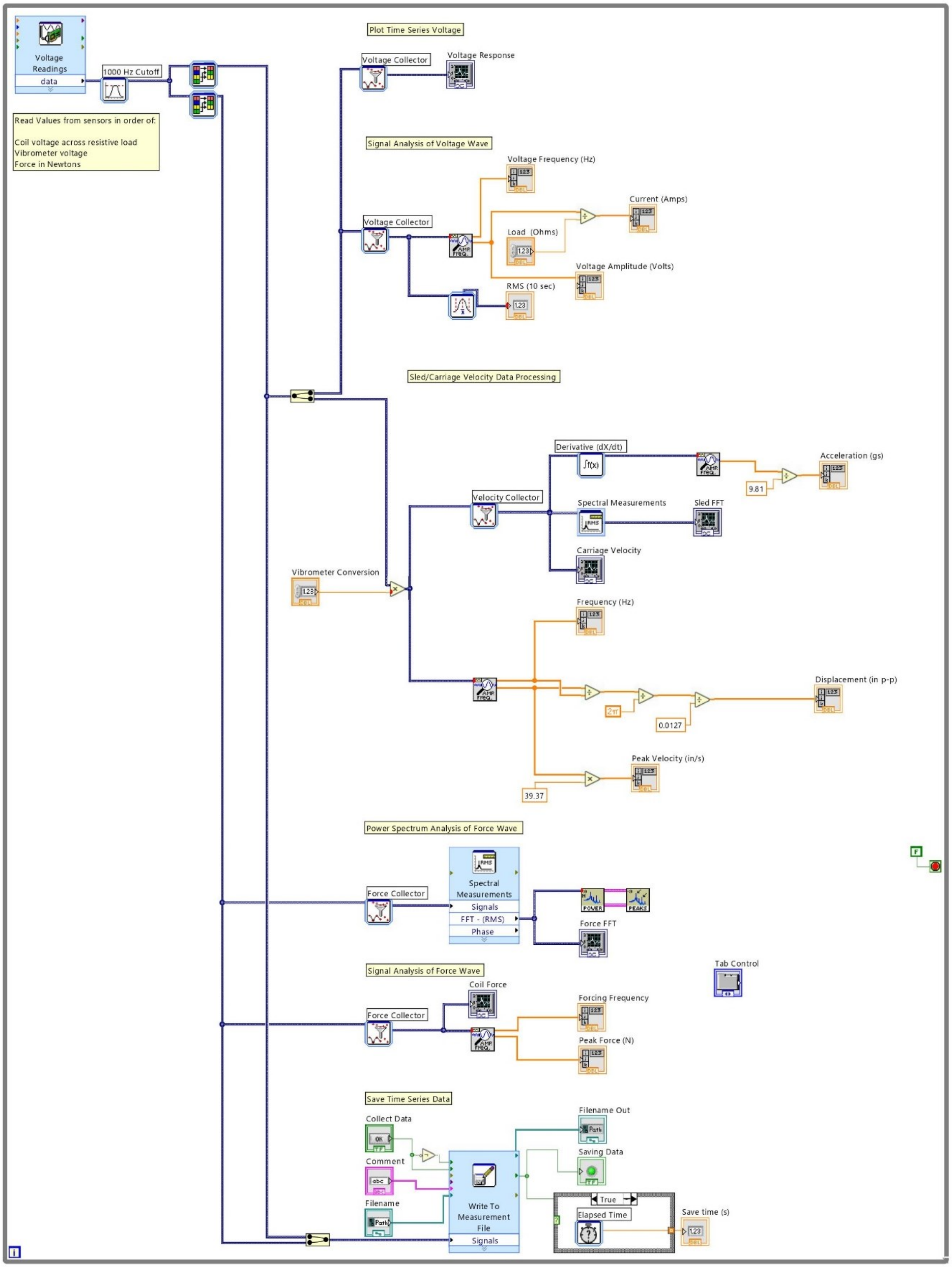

Figure C.1. Block diagram of the shaker table VI used to collect and analyze the time series carriage velocity, voltage across a resistive load, and electromagnetic force.

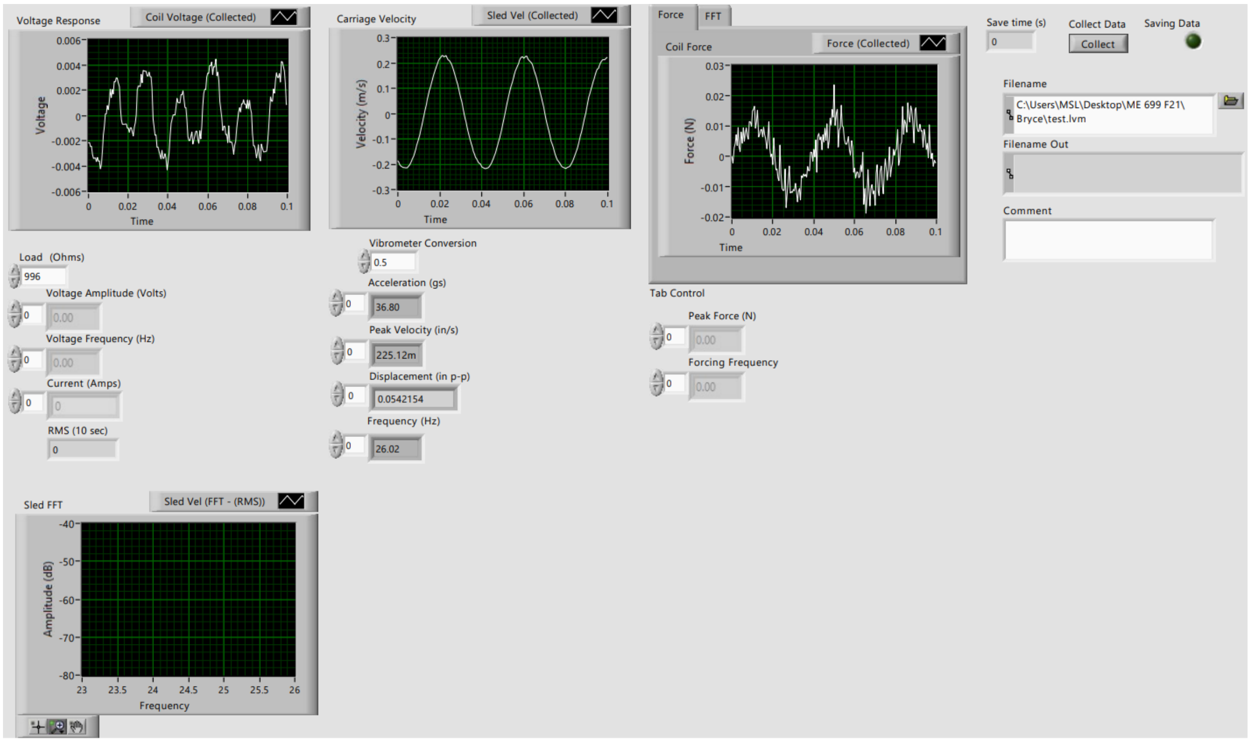

Figure C.2. Front panel of the shaker table VI used to display the analysis of the time series carriage velocity, voltage across a resistive load, and electromagnetic force in real time.